Charged-phonon theory and Fano effect in the optical spectroscopy of bilayer graphene

E. Cappelluti,[1,2] L. Benfatto,[2,3] M. Manzardo,[4] and A. B. Kuzmenko[5]

[1]*Instituto de Ciencia de Materiales de Madrid, CSIC, Madrid, Spain*
[2]*Institute for Complex Systems, U.O.S. Sapienza, CNR, Roma, Italy*
[3]*Dipartimento di Fisica, Università "La Sapienza," Roma, Italy*
[4]*Institute for Theoretical Solid State Physics, IFW Dresden, Helmholtzstr. 20, 01069 Dresden, Germany*
[5]*DPMC, Université de Genève, 1211 Genève, Switzerland*

Since their discovery, graphene-based systems represent an exceptional playground to explore the emergence of peculiar quantum effects. The present paper focuses on the anomalous appearance of strong infrared phonon resonances in the optical spectroscopy of bilayer graphene and on their pronounced Fano-like asymmetry, both tunable in gated devices. By developing a full microscopic many-body approach for the optical-phonon response we explain how both effects can be quantitatively accounted for by the quantum interference of electronic and phononic excitations. We show that the phonon modes borrow a large dipole intensity from the electronic background, the so-called charged-phonon effect, and at the same time interfere with it, leading to a typical Fano response. Our approach allows one to disentangle the correct selection rules that control the relative importance of the two (symmetric and antisymmetric) relevant phonon modes for different values of the doping and/or of the gap in bilayer graphene. Finally, we discuss the extension of the same theoretical scheme to the Raman spectroscopy, to explain the lack of the same features on the Raman phononic spectra. Besides its remarkable success in explaining the existing experimental data in graphene-based systems, the present theoretical approach offers a general scheme for the microscopic understanding of Fano-like features in a wide variety of other systems.

PACS number(s): 78.30.−j, 78.20.Ek, 78.67.Wj

I. INTRODUCTION

The peculiar properties of single and multilayer graphenes make these systems the promising basis for the future generation of electronic devices. Within this context, the analysis of the spectral properties of the phonon anomalies observed by means of different optical probes has provided a powerful tool not only for the characterization of the samples but also for the investigation of the underlying scattering mechanisms related to the electron-lattice interaction. A large part of the investigation along this line has been based on Raman spectroscopy.[1–10] Typical main features under investigation within this context were the frequency and the linewidth of the phonon anomalies, whose trend as a function of doping was found to be in good agreement with what is expected from the theoretical calculations of the phonon self-energy.[11,12] As an alternative route, phonon peak anomalies at $\omega \approx 0.2$ eV were detected also in the midinfrared optical conductivity of bilayer graphene.[13,14] Quite interestingly, unlike in the Raman spectroscopy, in this case a strong dependence of the phonon peak intensity as well as of its line-shape asymmetry on the gate voltage was reported. Understanding and controlling the mechanisms responsible for these features at relatively small doping and perpendicular electric fields is of fundamental importance.

From a theoretical point of view, the very evidence of a strong infrared (IR) phonon activity, such as the one reported in Refs. 13 and 14, can be considered puzzling in graphenes which, having atoms of only one specie (carbon), present a very small intrinsic dipole. In bilayer graphene, for instance, there are four carbon atoms in the unit cell, as depicted in Fig. 1, where atoms B_1 and A_2 are connected by the vertical hopping γ_1. There are two in-plane optical modes: an infrared-active antisymmetric (A) E_u mode, which corresponds to (out-of-phase) lattice displacements in the two layers [Fig. 1(a)];

and a symmetric (S) E_g mode, which is associated with in-phase displacements and is Raman active [Fig. 1(b)]. If the two layers were completely decoupled, all the atoms would be exactly equivalent to each other. It is thus clear by direct inspection that, although allowed by symmetry, the E_u mode would not induce any dipole and hence it would have no IR intensity. Beyond this simple model of decoupled layers, in real systems, the interlayer hopping would induce a slight inequivalence between the atoms (A_1, B_2) and atoms (A_2, B_1) and hence a finite electrical dipole under the E_u lattice displacements. The static dipole associated with such physics is however three orders of magnitude smaller than what is experimentally observed,[13] so that this effect alone cannot account for the huge increase of the phonon intensity upon gate-induced doping reported in Ref. 13.

A guideline to understanding the origin of this huge enhancement comes from the comparison with other carbon-based compounds, like fullerenes, where also a similar increase of the phonon intensity upon (chemical) doping was observed. This effect was explained in those materials in terms of a charged-phonon theory.[15,16]

The basic idea of the charged-phonon model can be understood by considering the electronic current (j) response function,

$$\chi_{jj}(\omega) = -\int dt \langle T_t j(t) j(0) \rangle \exp[i\omega t], \qquad (1)$$

which is related, within the Kubo approach, to the optical conductivity as

$$\sigma(\omega) \approx -\frac{\chi_{jj}(\omega)}{i\hbar\omega}. \qquad (2)$$
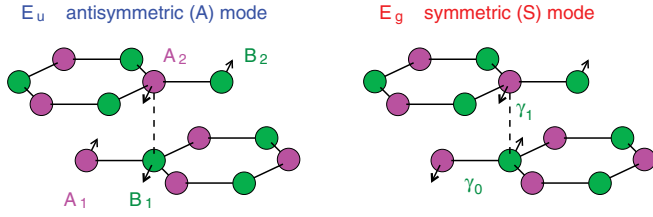
FIG. 1. (Color online) Atomic structure of bilayer graphene and lattice displacements for the E_u antisymmetric (A) phonon mode and for the E_g symmetric (S) mode. Labels denote the A and B sublattice in each plane. Solid links between atoms represent the in-plane γ_0 hopping, vertical dashed links the interplane hopping γ_1.

A typical diagram contributing to the electronic background at the lowest order is depicted in Fig. 2(a), corresponding to the single-bubble approximation. Effects of the electron-phonon interaction *on the electronic background* are commonly taken into account by replacing the noninteracting Green's functions in Fig. 2(a) with the Green's functions evaluated in the presence of electron-phonon interaction.[17,18] These processes lead to a smearing of the optical features and to a redistribution of the optical spectral weight. They are however not associated with the onset of resonances at the characteristic phonon energies in the optical conductivity.

A most interesting class of diagrams, analyzed by M. J. Rice in the context of the charged-phonon effect, is depicted in Fig. 2(b). Their contribution to the resulting optical conductivity can be described as[15,16]

$$\Delta\chi_{jj}(\omega) = |\chi_{j\mathrm{ph}}(\omega)|^2 D_{\mathrm{ph}}(\omega), \tag{3}$$

where $D_{\mathrm{ph}}(\omega)$ is the phonon propagator of the IR active phonon mode considered, and $\chi_{j\mathrm{ph}}(\omega)$ is the "mixed" response function between the current and the electron-phonon scattering operators (see Sec. II for a more detailed definition). The resulting optical conductivity of this contribution is thus proportional to the phonon propagator of the optically coupled lattice vibrations, and it presents typical resonances at the corresponding phonon frequencies.

It is worth stressing that the phonon becomes here optically visible thanks to an intermediate process [$\chi_{j\mathrm{ph}}(\omega)$] where the light couples to particle-hole electronic excitations. The function $\chi_{j\mathrm{ph}}$ acts therefore as a prefactor of the magnitude of the electronically induced phonon resonances. Pristine fullerenes and organic materials, for which the charged-phonon theory was originally proposed,[15,16] in the absence of doping, are semiconductors with a band gap significantly larger than the phonon energies. In this case the complex function $\chi_{j\mathrm{ph}}$ can be reasonably assumed to be real and proportional to

the charge concentrations n,

$$\Delta\chi_{jj}(\omega) \propto n D_{\mathrm{ph}}(\omega). \tag{4}$$

Equation (4) summarizes in a nutshell the essence of the charged-phonon effect, where the infrared phonon activity is triggered in by the coupling of a lattice mode ν with the optically allowed electronic particle-hole excitations.[15,16] As it was shown in Ref. 19, the physics underlying the charged-phonon effects is intimately related to the onset of Fano-like line-shape asymmetries.[20] Such unified charged-phonon-Fano theory was also employed to analyze the spectral properties of infrared optical phonon in pristine graphite[21] and in multilayer graphenes with different stacking orders.[22]

The purpose of the present paper is to provide a detailed microscopic derivation of the charged-phonon effect in the optical spectroscopy of graphenes. To this aim we focus on bilayer graphene as the simplest and paradigmatical example. We will show how all the information related to the phonon intensity and Fano asymmetry can be evaluated in terms of a unique quantity: the current/electron-phonon response function $\chi_{j\nu}$. Within this context we evaluate the dependence of the optical properties of the phonon resonance on microscopical parameters tunable by means of external gating. The correspondence between the Fano theory and the charged-phonon effect is derived microscopically, and a generalization of the charged-phonon effect to the Raman response is also provided.

The structure of the paper is the following. In Sec. II we summarize the main concepts of the charged-phonon theory and introduce the mathematical tools employed. In Sec. III we present an analytical discussion about the correspondence between the Fano and the charged-phonon theories, and a suitable quantification of the optical properties of the phonon resonances is introduced. The detailed evaluation of the infrared properties in the specific case of ungapped bilayer graphene is presented in Sec. IV, which is generalized in Sec. V to the case of gapped bilayer graphene in the presence of external gate voltage. The role of the electronic structure and of the breaking of particle-hole symmetry in the band structure is discussed in Sec. VI in bilayer graphene and compared with bulk graphite. A generalization of the charged-phonon theory and of the Fano interference analysis for the Raman spectroscopy, within an effective-mass approximation, is finally presented in Sec. VII. A summary of the present work and conclusion can be found in Sec. VIII. Appendixes A and B provide all the details of the analytical evaluation of the charge-phonon theory for IR spectroscopy of the ungapped bilayer graphene in the clean limit, and details about a suitable generalization for the Raman response.
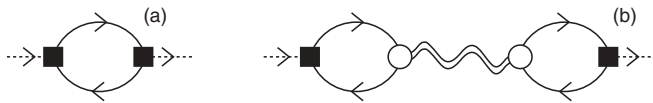

FIG. 2. (a) Lowest-order contribution to the current-current response function. (b) Diagrams involved in the charged-phonon effect. Solid and wavy lines are electronic and phonon propagators, respectively, white circles are the electron-phonon scattering operator while black squares represent here the current operator that couples light (dashed lines) to the particle-hole excitations.

II. CHARGED-PHONON THEORY IN BILAYER GRAPHENE

In order to apply at a quantitative level the concepts of the charged-phonon theory in graphenes, in this section we introduce the electronic band structure and the electron-phonon Hamiltonians as well as the relevant response functions which will provide the analytical tools to investigate the properties of the phonon peaks in the optical conductivity and in the Raman response. We focus here on the bilayer system as the most

simple and representative since the single-layer graphene does not present any IR phonon mode. We work in the 4×4 basis of the atomic orbitals, as depicted in Fig. 1(a). We introduce the four-vector defined as $\Psi_{\mathbf{k},\sigma}^{\dagger} = (a_{1\mathbf{k},\sigma}^{\dagger}, b_{1\mathbf{k},\sigma}^{\dagger}, a_{2\mathbf{k}\sigma}^{\dagger}, b_{2\mathbf{k}\sigma}^{\dagger})$, where $a_{i\mathbf{k},\sigma}^{\dagger}$ and $b_{i\mathbf{k},\sigma}^{\dagger}$ operators create an electron with spin σ in the layer i and on the sublattice A or B, respectively.

Considering for simplicity a simple γ_0-γ_1 model, and including a possible asymmetry between upper and lower layer induced by a gate voltage, we can write the noninteracting electronic Hamiltonian as

$$H_0 = \sum_{\mathbf{p},\sigma} \Psi_{\mathbf{p},\sigma}^{\dagger} \hat{H}_{\mathbf{p}} \Psi_{\mathbf{p},\sigma}, \tag{5}$$

where

$$\hat{H}_{\mathbf{p}} = \begin{pmatrix} \Delta/2 & \gamma_0 f_{\mathbf{p}} & 0 & 0 \\ \gamma_0 f_{\mathbf{p}}^* & \Delta/2 & \gamma_1 & 0 \\ 0 & \gamma_1 & -\Delta/2 & \gamma_0 f_{\mathbf{p}} \\ 0 & 0 & \gamma_0 f_{\mathbf{p}}^* & -\Delta/2 \end{pmatrix}, \tag{6}$$

γ_0, γ_1 are the nearest-neighbor in-plane and interplane tight-binding hopping parameters, respectively, and $f_{\mathbf{p}} = e^{-ip_x a/\sqrt{3}} + 2e^{ip_x a/2\sqrt{3}} \cos(p_y a/2)$.

Close to the $K = (4\pi/3a, 0)$ point, writing $\mathbf{p} = K + \mathbf{k}$, and linearizing around the K point, we can also write

$$\hat{H}_{\mathbf{k}} = \begin{pmatrix} \Delta/2 & v\pi_- & 0 & 0 \\ v\pi_+ & \Delta/2 & \gamma_1 & 0 \\ 0 & \gamma_1 & -\Delta/2 & v\pi_- \\ 0 & 0 & v\pi_+ & -\Delta/2 \end{pmatrix}. \tag{7}$$

Here $v = 10^6$ m/s is the Fermi velocity for single-layer graphene, $\gamma_1 = 0.39$ eV is the interlayer hopping, Δ is the electrostatic energy difference between the layers and $\pi_\pm = \hbar(k_x \pm ik_y)$. The electronic Green's function in the imaginary space is thus expressed as a 4×4 matrix, $\hat{G}(\mathbf{k}, i\omega_n) = 1/[(i\hbar\omega_n + \mu)\hat{I} - \hat{H}_{\mathbf{k}}]$, where μ is the chemical potential and $\hbar\omega_n = \pi T(2n + 1)$ are fermionic Matsubara frequencies. The electronic bands $E_{\mathbf{k},n}$ are obtained from the diagonalization of Eq. (7),

$$E_{\mathbf{k}}^2 = \frac{\gamma^2}{2} + \frac{\Delta^2}{4} + (\hbar v k)^2 \pm \sqrt{\frac{\gamma^4}{4} + (\hbar v k)^2(\gamma^2 + \Delta^2)}, \tag{8}$$

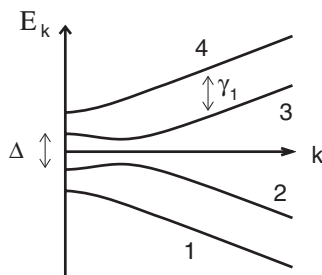and are labeled according to Fig. 3.

FIG. 3. Scheme of the band structure close to the K point. The interlayer hopping parameter γ_1 determines the splitting at high energy of bands 3 and 4. The interlayer different potential Δ determines the size of the energy gap at the K ($\mathbf{k} = 0$) point.

We can also define the current operator $j_\alpha = (1/N)\sum_{\mathbf{k},\sigma} \Psi_{\mathbf{k},\sigma}^{\dagger} \hat{j}_{\mathbf{k},\alpha} \Psi_{\mathbf{k},\sigma}$, where $\alpha = x, y$, N is the total number of unit cells, and where

$$\hat{j}_{\mathbf{k},\alpha} = -\frac{e}{\hbar} \frac{d}{dk_\alpha} \hat{H}_{\mathbf{k}}. \tag{9}$$

In particular, focusing on the current operator along the y axis, from Eqs. (5)–(7) we get

$$\hat{j}_{\mathbf{k},y} = -ev\hat{I}(\hat{\sigma}_y), \tag{10}$$

where $\hat{A}(\hat{B}) \equiv \hat{A} \otimes \hat{B}$.

The electron-phonon Hamiltonian describing electrons interacting with the optical modes has also been discussed by several authors.[12,23,24] As mentioned above, in bilayer graphene there are two optical in-plane phonons at $\mathbf{q} = 0$ (see Fig. 1): the E_g symmetric (S) mode and the antisymmetric (A) E_u one. In the absence of a potential difference between the two layers, the first one is Raman active while the second one is infrared active. The relative displacement of the two sublattice atoms A and B in the first layer is given for example by

$$\mathbf{u}_\nu(\mathbf{r}) = \sum_{\mathbf{q},\mu} \sqrt{\frac{\hbar^2}{4M\hbar\omega_0}} (c_{\mathbf{q},\mu} + c_{-\mathbf{q},\mu}^{\dagger}) \mathbf{e}_\mu(\mathbf{q}) e^{i\mathbf{q}\cdot\mathbf{r}}. \tag{11}$$

M is the mass of a carbon atom, ω_0 is the phonon frequency at the Γ point, $\mu = t, l$ denotes the polarization (transverse or longitudinal), and $c_{\mathbf{q},\mu}$ and $c_{\mathbf{q},\mu}^{\dagger}$ are the phonon creation and annihilation operators, respectively. Using $q_x = q\cos\phi(\mathbf{q})$ and $q_y = q\sin\phi(\mathbf{q})$ the polarization vectors $\mathbf{e}_\mu(\mathbf{q})$ are given by $\mathbf{e}_l(\mathbf{q}) = i(\cos\phi(\mathbf{q}), \sin\phi(\mathbf{q}))$ and $\mathbf{e}_t(\mathbf{q}) = i(-\sin\phi(\mathbf{q}), \cos\phi(\mathbf{q}))$. Following Ref. 12 the interaction between the optical phonons and the electrons at the K point can be written as

$$H_{int} = -\sqrt{2}\frac{\beta\hbar v}{b^2} \sigma^{(\pm)} \times \mathbf{u}_\nu(\mathbf{r}), \tag{12}$$

where $\sigma^{(+)} = \hat{I}(\hat{\sigma})$, $\sigma^{(-)} = \hat{\sigma}_z(\hat{\sigma})$, $b = 1.42$ Å is the in-plane carbon-carbon nearest-neighbor distance, and β is a dimensionless parameter related to the deformation potential, whose typical value is $\beta = 2.88$.[25,26] In the following we shall consider the case of an electric field along the y axis, so that only the lattice vibrations along the y direction will couple to the light. Since for $\mathbf{q} \to 0$ the result is independent on $\phi(\mathbf{q})$, we take $\phi(\mathbf{q}) = 0$, so that only the $\mathbf{e}_t$ polarization vector has a component along y. As a consequence we can write, close to the K point, the electron-phonon interaction for the $\nu = $ A,S mode as

$$H_\nu = \sum_{\mathbf{k},\sigma} \Psi_{\mathbf{k}+\mathbf{q},\sigma}^{\dagger} \hat{V}_\nu(\mathbf{q}) \Psi_{\mathbf{k},\sigma} e^{i\mathbf{q}\cdot\mathbf{r}} (c_{\mathbf{q},\mu} + c_{-\mathbf{q},\mu}^{\dagger}), \tag{13}$$

where

$$\hat{V}_A(\mathbf{q} \to 0) = ig\hat{\sigma}_z(\hat{\sigma}_x), \tag{14}$$

$$\hat{V}_S(\mathbf{q} \to 0) = ig\hat{I}(\hat{\sigma}_x), \tag{15}$$

and where $g = (\beta\hbar v/b^2)\sqrt{\hbar^2/2M\hbar\omega_0} = 0.27$ eV. Note that, since $\mathbf{e}_t(\mathbf{q}) = -\mathbf{e}_t(-\mathbf{q})$, one has that $\lim_{\mathbf{q}\to 0} \hat{V}_\nu(-\mathbf{q}) = -\lim_{\mathbf{q}\to 0} \hat{V}_\nu(\mathbf{q})$.

We have now all the tools to investigate the full optical properties. In this regard it is convenient to define the generic propagator for bosonic operators A and B as

$$\chi_{AB}(i\omega_m) = -\int_0^{1/T} d\tau \langle T_\tau A(\tau)B(0)\rangle \exp[i\omega_m\tau], \quad (16)$$

where τ is the imaginary time, T_τ is the time-ordering operator, and $\hbar\omega_m = 2\pi mT$ is the bosonic Matsubara frequency.

The complex electronic optical conductivity per layer $\sigma(\omega)$ is obtained from the analytical continuation of $\chi_{jj}(i\omega_m)$ to the real axis ($i\omega_m \to \omega + i0^+$):

$$\sigma(\omega) = -\frac{\hbar}{V^{3D}}\frac{\chi_{jj}(\omega + i0^+)}{i\hbar\omega}, \quad (17)$$

where $V^{3D} = 2dS_{cell}^{2D}$ with $d = 3.35$ Å being the interlayer distance and $S_{cell}^{2D} = \sqrt{3}a^2/2$ the two-dimensional area of the graphene unit cell, with $a = 2.46$ Å.

At the lowest noninteracting order, the current-current response function $\chi_{jj}(i\omega_m)$ reduces to the single-bubble approximation depicted in Fig. 2(a):

$$\chi_{jj}(i\omega_m) = N_s N_v \frac{T}{N}\sum_{\mathbf{k},n} \text{Tr}[\hat{j}_y \hat{G}_0(\mathbf{k}, i\omega_n + i\omega_m)$$
$$\times \hat{j}_y \hat{G}_0(\mathbf{k}, i\omega_n)], \quad (18)$$

where $N_s = N_v = 2$ are the spin and valley degeneracies, respectively, and $\hat{G}_0(\mathbf{k}, i\omega_n)$ is the 4×4 noninteracting electron Green's function which, in the orbital basis, is not diagonal. As a consequence, the retarded response function $\chi_{jj}(\omega)$ will have contributions coming from both the interband and intraband electronic excitations. In general it can be decomposed as

$$\chi_{jj}(\omega) = \sum_{\alpha,\beta=1}^4 \chi_{jj}^{\alpha\beta}(\omega), \quad (19)$$

where α, β are the band indexes and $\chi_{jj}^{\alpha\beta}(\omega)$ describes the intraband ($\alpha = \beta$) or interband ($\alpha \neq \beta$) particle-hole excitations contributing to the total χ_{jj}. The properties of the optical conductivity in gated bilayer graphene has been theoretically investigated in detail in Ref. 27 and experimentally confirmed in Refs. 28–31. One can see that, at the phonon energies $\omega \approx 0.2$ eV, only the 2–3 interband transitions contribute to $\chi_{jj}''(\omega)$ (and therefore to the optical electronic background).[27] Such background could be modulated by the charge doping (and therefore by the applied gate voltage) so that it drastically vanishes for $2|\mu| \gtrsim 0.2$ eV. Within the commonly widespread idea, one would expect that this is the electronic background that controls the q Fano parameter and then the asymmetry of the phonon peak. However, as we shall see below, a correct application of Fano theory to graphene leads to a different characteristic electronic response function related to the Fano effect seen in several experiments.

Optical properties of the phonon resonances can be investigated with the charged-phonon theory by analyzing the diagrams in Fig. 2(b). In ungated samples, only one phonon, the E_u antisymmetric mode, is expected to be IR active. We can write thus

$$\Delta\chi_{jj}(\omega) = \chi_{jA}(\omega)D_{AA}(\omega)\chi_{A^\dagger j}(\omega), \quad (20)$$

where χ_{jA} is the mixed response function between the current operator j_y and the electron-phonon scattering operator V_A.

However, in the most general case of gated samples with $\Delta \neq 0$, also the symmetric E_g mode acquires a finite IR activity.[13,14] We can write then

$$\Delta\chi_{jj}(\omega) = \chi_{jA}(\omega)D_{AA}(\omega)\chi_{A^\dagger j}(\omega) + \chi_{jS}(\omega)D_{SS}(\omega)\chi_{S^\dagger j}(\omega)$$
$$+ [\chi_{jA}(\omega)D_{AS}(\omega)\chi_{S^\dagger j}(\omega) + \text{H.c.}], \quad (21)$$

where $\nu = A, S$.

Equations (21) can be completed with the Dyson's equation for the phonon Green's functions $D_{\nu\nu'}$:[23,24]

$$[D^{-1}(\omega)]_{\nu\nu'} = \delta_{\nu,\nu'}[D_0^{-1}(\omega)] - \chi_{\nu^\dagger\nu'}(\omega), \quad (22)$$

where $D_0(\omega) = -2\hbar\omega_0/[\hbar^2\omega_0^2 - (\hbar\omega + i0^+)^2]$ is the phonon propagator in the absence of electron-phonon interaction and $\chi_{\nu^\dagger\nu'}(\omega)$ provides the matrix components of the phonon self-energy. The quantity ω_0 represents the bare phonon frequencies for a generic mode ν in the absence of electron-phonon interaction, and it is assumed here to be degenerate $\omega_{0A} = \omega_{0S} = \omega_0$. As has been discussed in detail in Refs. 23, 24, and 32, the mixing between the A and S modes (mediated by the self-energy χ_{AS}) is only active when $\Delta \neq 0$. In this case the phonon eigenmodes do not correspond any more to symmetric/antisymmetric vibrations of the atoms in neighboring layers, so that each A and S propagator has a double-pole structure, centered at the values $\omega_\pm$ of the phonon eigenfrequencies.

Equations (21) and (22) provide the theoretical tools needed to evaluate microscopically the onset and the properties of phonon peaks in the optical conductivity. In general, all the information about *frequencies* and *lifetimes* of phonons is encoded in the phonon self-energy $\chi_{\nu^\dagger\nu'}$ whereas the mixed (current/electron-phonon interaction) response functions $\chi_{j\nu}$ are related to the *intensity* and to the possible *Fano asymmetry* of the phonon peaks, as we shall discuss in the next section.

III. CORRESPONDENCE WITH THE STANDARD FANO THEORY

In order to better clarify the connection between Eq. (21) and the standard Fano theory let us consider first the case $\Delta = 0$, where only the A mode is optically active and the expression (21) reduces to Eq. (20). In addition, for $\Delta = 0$ the mixed phonon self-energy $\chi_{A^\dagger S}$ vanishes, which means that the A and S modes coincide with the eigenmodes for the lattice vibrations. In particular, this implies that the phonon propagator D_{AA} has a single resonance, and the main effect of the phonon self-energy is to induce a shift of the phonon frequency $\hbar\omega_A = \hbar\omega_0 + \text{Re}\chi_{A^\dagger A}(\omega_A)$ and a finite line broadening $\Gamma_A = -\text{Im}\chi_{A^\dagger A}(\omega_A)$. Therefore for $\omega \approx \omega_A$ we can approximate the phonon propagator as

$$D_{AA}(\omega) = \frac{1}{\hbar(\omega - \omega_A) + i\Gamma_A}. \quad (23)$$

Using the relation $\chi_{A^\dagger j}(\omega) = \chi_{jA}(\omega)$, the optical conductivity can be expressed in terms of the real and imaginary part of the mixed response function χ_{jA} and of the propagator (23). In particular, introducing the variable $z = \hbar[\omega - \omega_A]/\Gamma_A$ we have $\text{Re}D_{AA} = D'_{AA} = z/\Gamma_A(1 + z^2)$ and $\text{Im}D_{AA} = D''_{AA} =$

$-1/\Gamma_A(1+z^2)$, so that

$$\text{Im}\Delta\chi_{jj} = D''_{AA}[(\chi'_{jA})^2 - (\chi''_{jA})^2] + 2D'_{AA}\chi'_{jA}\chi''_{jA}$$

$$= -\frac{(\chi'_{jA})^2 - (\chi''_{jA})^2 - 2z\chi'_{jA}\chi''_{jA}}{\Gamma_A(1+z^2)}. \tag{24}$$

As a consequence, the real part of the optical conductivity (17) close to the resonance frequency ω_A can be written as[19]

$$\text{Re}\Delta\sigma(\omega)|_{\omega\approx\omega_A} \approx I_A\left[\frac{q_A^2 - 1 + 2q_A z}{q_A^2(1+z^2)}\right], \tag{25}$$

where we defined the Fano parameter q as

$$q_A = -\frac{\chi'_{jA}(\omega_A)}{\chi''_{jA}(\omega_A)}, \tag{26}$$

while the prefactor is given by

$$I_A = \frac{[\chi'_{jA}(\omega_A)]^2}{\omega_A\Gamma_A V}. \tag{27}$$

As one can see, Eq. (25) reproduces the Fano formula, where the q parameter controls the asymmetry of the peak with respect to a standard Lorentzian profile, that is recovered in the limit of $q \to \infty$. As observed already in Ref. 19, the derivation of Eqs. (25) and (26) shows that the Fano effect stems from a correct implementation of the charged-phonon theory. Therefore, for the sake of simplicity, in the following we shall regard the phonon properties (intensity and line-shape asymmetry) arising from this common nature as the "Fano-Rice" effect. Moreover, the above set of equations provides a general scheme to calculate microscopically the relevant parameters that control the shape and the intensity of the phonon peak, in particular q_A and I_A, that are fully determined once that the mixed response function χ_{jA} is computed.

Before showing explicitly the calculation of χ_{jA} we would like to make a more direct comparison with the standard Fano formalism[20] that is often quoted in the literature. Following the original work by Fano,[20] the asymmetry parameter q that measures the interference effect between a discrete phonon state $|\phi\rangle$ of energy ω_0 and a continuum of electronic states $|\psi_\omega\rangle$ can be written as

$$q = \frac{\langle\phi|T|i\rangle + P\int d\omega'\frac{V_{\omega'}\langle\psi_{\omega'}|T|i\rangle}{\omega_0-\omega'}}{\langle\psi_{\omega_0}|T|i\rangle\pi V_{\omega_0}}, \tag{28}$$

where P denotes the principal part of the integral, and V_ω measures the hybridization between the phonon and the electronic states at the energy ω, $V_\omega = \langle\psi_\omega|H|\phi\rangle$. Here $\langle f|T|i\rangle$ denotes in general the transition amplitude from an initial state $|i\rangle$ and a final state $|f\rangle$. The first term in the numerator of Eq. (28) represents the response of the bare phonon state, i.e., the bare dipole of the system under the lattice distortion, while the second one gives the contribution coming from the electronic excitations. Note that the relevant electronic excitations are not restricted to the vicinity of the phonon frequency ω_0 but they involve higher energy states ω' as well. In contrast, the denominator depends solely on the processes at $\omega = \omega_0$ and it vanishes if there is no electronic continuum at the phonon energy, so that in this case $q = \infty$ and no Fano asymmetry is expected. In ordinary systems the bare phonon intensity $\langle\phi|T|i\rangle$ is large,

so that q becomes appreciably small only in the presence of a considerable electron-phonon coupling V_{ω_0}, and the observation of a pronounced Fano asymmetry is considered as a signature of large electron-phonon interactions.[33] However, the case of graphene is radically different: since here the bare phonon activity is negligible, the main phonon intensity comes from the particle-hole excitations (Rice effect), and the Fano asymmetry can be pronounced even in the presence of a relatively small electron-phonon coupling. In order to show this more explicitly, we introduce the complex function:

$$\chi(\omega) = \int d\omega'\frac{C(\omega')}{\omega-\omega'+i\eta}, \tag{29}$$

where we defined

$$C(\omega) = V_\omega\langle\psi_\omega|T|i\rangle. \tag{30}$$

For $\langle\phi|T|i\rangle \approx 0$, Eq. (28) can be written as

$$q = -\frac{\chi'(\omega_0)}{\chi''(\omega_0)}, \tag{31}$$

which reduces to Eq. (26) derived above from the charged-phonon theory. Note that both χ' and χ'' are proportional to the electron-phonon matrix element V_ω (i.e., g in our previous notation), so that the strength of the electron-phonon interaction cancels out in Eq. (31) as well as in (26). As we shall see below, the response function χ_{jA} has exactly the form of Eq. (29), and we will be able to compute explicitly the function $C(\omega)$.

A few more final observations are in order concerning Eqs. (25)–(33). First, in contrast to the ordinary case where also the bare dipole charge of the phonon must be considered, in the case of graphene the two quantities q_A, I_A are not independent. This is again a consequence of a correct implementation of the charged-phonon effect, i.e., of the fact that in graphene the optical activity of the phonon is fully borrowed from the electronic excitations. This also permits us to quantify the "strength" of a phonon resonance in the optical conductivity on a more rigorous ground. To this aim, for a given phonon mode ν, two typical quantities are considered in the literature: the integrated spectral area

$$W'_\nu = \int d\omega\text{Re}\Delta\sigma(\omega), \tag{32}$$

and the phonon intensity W_ν, as obtained from the Fano-like fit in Eq. (25) as

$$W_\nu = \pi\Gamma_\nu I_\nu. \tag{33}$$

The quantity W_ν is considered to be the "bare" spectral intensity that the mode would have in the absence of the Fano interference. It is straightforward to show that these two quantities are related by the formula

$$W'_\nu = \left(1 - \frac{1}{q_\nu^2}\right)W_\nu, \tag{34}$$

so that $W' \to W_\nu$ when $|q_\nu| \to \infty$ for a symmetric Lorentzian profile [Fig. 4(a)].

Both W_ν and W'_ν can be expressed in the common Fano-charged-phonon framework via the mixed response
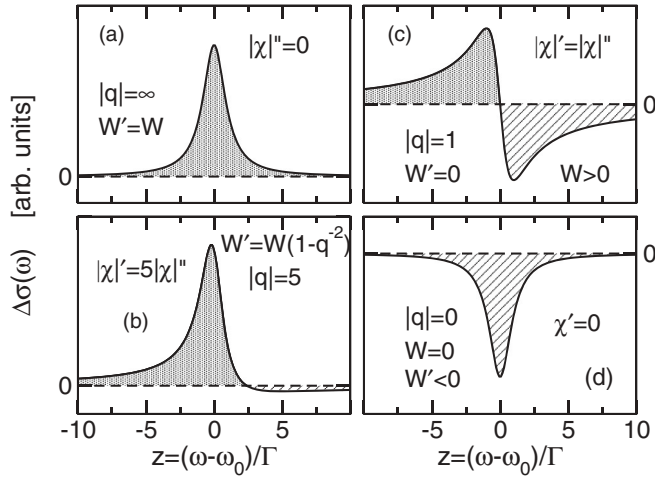
FIG. 4. Sketch of the optical properties of a phonon resonance in different characteristic regimes: (a) positive symmetric Lorentzian peak $[|q| = \infty; |\chi''_{j\nu}(\omega_\nu)| = 0]$, where $W = W'$; (b) weak asymmetric Fano profile [ex.: $|q| = 5$; $|\chi'_{j\nu}(\omega_\nu)| = 5|\chi''_{j\nu}(\omega_\nu)|$]; (c) highly asymmetric case $[|q| = 1; |\chi'_{j\nu}(\omega_\nu)| = |\chi''_{j\nu}(\omega_\nu)|]$, where the integrated area $W' = 0$ because of the cancellation of positive and negative spectral regions; (d) negative phonon peak ($|q| = 0$; $\chi' \approx 0$), where the "bare" intensity vanishes, $W = 0$, although a phonon anomaly is visible in the imaginary part of χ. The total phonon strength P is the same in all the cases.

function $\chi_{j\nu}$:

$$W_\nu = \frac{\pi \chi'^2_{j\nu}(\omega_\nu)}{\omega_\nu} \quad (35)$$

and

$$W'_\nu = \frac{\pi \left[\chi'^2_{j\nu}(\omega_\nu) - \chi''^2_{j\nu}(\omega_\nu) \right]}{\omega_\nu}. \quad (36)$$

It should be however stressed that none of these two quantities, W, W', can provide a satisfactory quantification of the *magnitude* of the phonon optical anomaly. For instance, in the case $|q_\nu| \approx 1$, where the phonon peak asymmetry is strongest and which corresponds to $|\chi'_{j\nu}(\omega_\nu)| = |\chi''_{j\nu}(\omega_\nu)|$, we get $W'_\nu = 0$ due to the cancellation of positive and negative spectral regions [Fig. 4(c)]. On the other hand, when $\chi'_{j\nu}(\omega_\nu) \approx 0$, the spectral properties are characterized by a sizable *negative* Lorentzian peak whose intensity is driven by $\chi''_{j\nu}(\omega_\nu)$ whereas the estimated bare intensity is vanishingly small, $W_\nu \approx 0$ [Fig. 4(d)].

Both definitions W and W' thus fail to describe the actual magnitude of the optical-phonon resonance independently of its Fano-like properties. This problem can be solved however thanks to the microscopical identification of the optical properties in terms of the mixed response function $\chi_{j\nu}$. The simple identification of W and W' as $W_\nu \propto \chi'^2_{j\nu}$, $W'_\nu \propto \chi'^2_{j\nu} - \chi''^2_{j\nu}$ suggests us to introduce a strictly *positively defined* quantity,

$$P_\nu = \frac{\pi \left[\chi'^2_{j\nu}(\omega_\nu) + \chi''^2_{j\nu}(\omega_\nu) \right]}{\omega_\nu}, \quad (37)$$

which we refer to as *phonon strength*. Note that $P \to 0$ only when both $\chi'_{j\nu}, \chi''_{j\nu} \to 0$, i.e., when the phonon features are

indeed vanishingly small. In the following, when discussing the *magnitude* of an optical-phonon resonance, we shall therefore refer to this quantity P_ν, which permits us to describe the actual visibility of a phonon structure independently of its Fano shape. The robustness of the parameter P_ν to characterize the magnitude of the phonon resonance independently of its line shape and its Fano properties is demonstrated in Fig. 4 where all the panels were evaluated for fixed phonon strength.

As a last point we would like to stress that it is the mixed response function χ_{jA}, and not the electronic background χ_{jj}, as was considered in Refs. 15 and 16, that determines the phonon strength and the asymmetry. As we shall see, this makes a crucial difference. Indeed, while all the possible electronic excitations contribute to χ_{jj}, only a subset of them enters into the mixed response function χ_{jA} (and χ_{jS} in the case $\Delta \neq 0$), determining in this way the exact selection rules for the phonon activity in bilayer graphene.

IV. FANO-RICE PROPERTIES IN UNGAPPED BILAYER GRAPHENE ($\Delta = 0$)

In the case of unbiased graphene the mixed response function χ_{jA} can be computed analytically in the bare-bubble approximation, namely,

$$\chi_{j\nu}(i\omega_m) = N_s N_\nu \frac{T}{N} \sum_{\mathbf{k},n} \text{Tr}[\hat{j}_y \hat{G}(\mathbf{k}, i\omega_n + i\omega_m) \hat{V}_\nu \hat{G}(\mathbf{k}, i\omega_n)],$$
$$(38)$$

where we use in Eq. (38) the bare electronic Green's functions. Some additional details of the calculation are given in Appendix A. Due to the multiband structure of the system, χ_{jA} has the typical structure of a particle-hole Lindhard response function, with proper coherence factors C^{nm}_{jA} weighting the contributions of the various excitations between the n and m bands. In particular, using the explicit matrix expressions of the $\hat{j}$ and $\hat{V}_A$ operators, one gets

$$\chi_{jA}(\omega) = \chi^{12}_{jA}(\omega) + \chi^{13}_{jA}(\omega) - \chi^{24}_{jA}(\omega) - \chi^{34}_{jA}(\omega). \quad (39)$$

Here n,m are the band indexes and $\chi^{nm}_{jA}(\omega) = \pi^{nm}_{jA}(\omega) - \pi^{mn}_{jA}(\omega)$, where

$$\pi^{nm}_{jA}(\omega) = \frac{1}{N} \sum_{\mathbf{k}} C^{nm}_{jA,\mathbf{k}} \frac{f(E_{\mathbf{k},n} - \mu) - f(E_{\mathbf{k},m} - \mu)}{E_{\mathbf{k},n} - E_{\mathbf{k},m} + \hbar\omega + i\eta}, \quad (40)$$

and where

$$C^{nm}_{jA,\mathbf{k}} = gev N_s N_\nu \frac{\gamma_1}{4\sqrt{(\hbar vk)^2 + \gamma_1^2}} \quad (41)$$

for $(n,m) = (1,2),(1,3),(2,4),(3.4)$, and zero otherwise. In Eq. (40) μ represents the chemical potential, and η is a phenomenological parameter that accounts for the damping in the electronic states, so that the clean limit corresponds to $\eta \to 0$.[34] Note that, once we identify

$$C(\omega) = \frac{1}{N} \sum_{m,n} \sum_{\mathbf{k}} C^{nm}_{jA,\mathbf{k}} \delta(E_{\mathbf{k},n} - E_{\mathbf{k},m} + \hbar\omega)$$
$$\times [f(E_{\mathbf{k},n} - \mu) - f(E_{\mathbf{k},m} - \mu)], \quad (42)$$

the function $\chi_{jA}(\omega)$ can be written exactly as in Eq. (29) above, with the particle-hole energy difference $\omega' = E_{\mathbf{k},n} - E_{\mathbf{k},m}$

playing the role of the electronic continuum in the Fano theory. Thus our approach allows one to identify the optical intensity of the phonon peaks and their Fano parameters in terms of the real and imaginary parts of a specific response function, that can be calculated using the standard diagrammatic theory. This means in particular that we can determine (i) which phonon is coupled to the current, and (ii) which electronic excitations couple to each phonon mode.

All these elements can be quantified in an analytical way for the A phonon in the case of no gap. First of all, note that for $\mu = 0$ the term χ_{jA}^{13} cancels precisely with χ_{jA}^{24}, whereas χ_{jA}^{12}, χ_{jA}^{34} are both vanishing because particle-hole excitations between completely full or empty bands are not allowed. As a consequence $\chi_{jA}(\omega) = 0$, implying that the intensity of the A mode, although it has the correct symmetry, vanishes in undoped bilayer graphene.[35] As we shall see, this property holds true even in the presence of an interlayer difference potential Δ.

The total mixed response function $\chi_{jA}(\omega)$ as well as its single contributions $\chi_{jA}^{nm}(\omega)$ can be easily evaluated in the clean limit, $\eta = 0$, and in the linear approximation for the band dispersion, corresponding to the Hamiltonian given by Eq. (7). Details of the computation are also reported in Appendix A. It is convenient to introduce the dimensionless quantity $\xi(\omega)$,

$$\chi_{jA}(\omega) = A\xi(\omega),$$

where $A = ge\gamma S_{\text{cell}}^{\text{2D}}/4\pi\hbar^2 v$. At $T = 0$ we obtain the analytical expressions

$$\xi'(\omega) = \ln\left[\frac{(\gamma_1 + \hbar\omega)(\gamma_1 - \hbar\omega + 2|\mu|)}{(\gamma_1 - \hbar\omega)(\gamma_1 + \hbar\omega + 2|\mu|)}\right]$$
$$- \theta(|\mu| - \gamma_1)\ln\left[\frac{(\gamma_1 + \hbar\omega)(\gamma_1 + \hbar\omega - 2|\mu|)}{(\gamma_1 - \hbar\omega)(\gamma_1 - \hbar\omega - 2|\mu|)}\right]$$
$$+ \frac{4\hbar\omega[|\mu|\theta(\gamma_1 - |\mu|) + \theta(|\mu| - \gamma_1)]}{(\gamma_1^2 - \hbar^2\omega^2)}, \qquad (43)$$

$$\xi''(\omega) = \pi\{\theta(\hbar|\omega| - \gamma_1)\theta(\hbar|\omega| - 2|\mu| + \gamma_1)$$
$$- \theta(\hbar|\omega| - 2|\mu| - \gamma_1) + 2[|\mu|\theta(\gamma_1 - |\mu|)$$
$$+ \theta(|\mu| - \gamma_1)]\delta(\hbar|\omega| - \gamma_1)\}. \qquad (44)$$

The real and imaginary parts of $\chi_{jA}(\omega)$ for a representative case $n = 5 \times 10^{12}$ cm^{-2} ($\mu = 0.13$ eV) are shown in Fig. 5(a), whereas in panels (b)–(d) the contribution of the single interband transitions is also shown. It is interesting to remark that for $|\omega| \gtrsim \gamma_1 + 2|\mu|$ the term $\text{Im}\chi_{jA}^{13}(\omega)$ cancels exactly with $\text{Im}\chi_{jA}^{24}(\omega)$, so that only a limited low-frequency energy window $\gamma_1 \lesssim |\omega| \lesssim \gamma_1 + 2|\mu|$ contributes to the imaginary part (and hence, via Kramers-Kronig relations, to the real part) of the mixed response function χ_{jA}. This fact guarantees that the result is valid even if the calculation has been done using the linearized graphene bands instead of the full periodic band structure.

According to Eq. (25), the computation of the optical-phonon spectra requires the evaluation of the quantities (43) and (44) at the phonon frequency ω_A. In order to determine ω_A, one should in principle solve the phonon Dyson's equation (22). However, the shift of the renormalized phonon frequencies ω_ν is only a few meV, which is much smaller than $\omega_0 \approx 200$ meV, so that we can replace ω_A with ω_0. In any case,
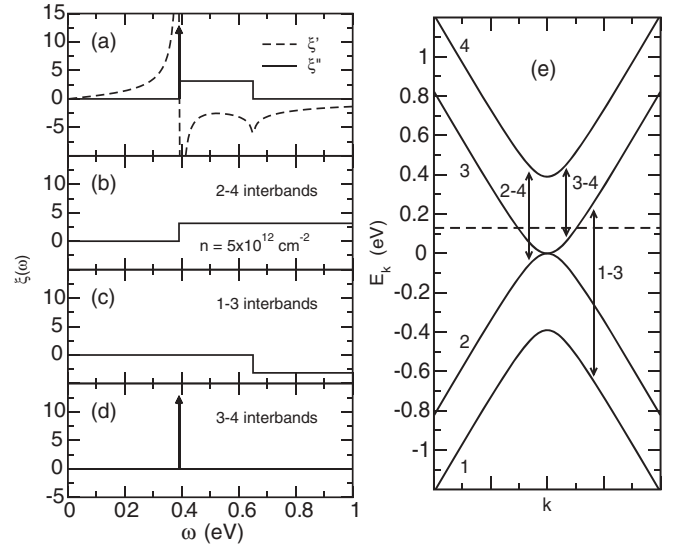

FIG. 5. (a) Real (dashed line) and imaginary (solid line) part of the dimensionless response functions $\xi(\omega)$ for $n = 5 \times 10^{12}$ cm^{-2} and $T = 0$. The vertical arrow for $\xi''(\omega)$ represents a δ function with spectral weight $2|\mu|$; see Eq. (44). (b)–(d) Contributions of the single interband transitions to the total $\xi''(\omega)$. (e) Sketch of the allowed particle-hole interband excitations. The horizontal dashed line marks here the chemical potential.

as one can see in Eq. (39), since the low-energy 2–3 interband transitions are not allowed in χ_{jA}, the lowest threshold for the particle-hole excitations is determined in the clean limit $\eta = 0$ by the 1–3 interband transitions with $\omega > \gamma_1 = 0.39$ eV, so that $\text{Im}\chi_{jA}(\omega_A) = 0$. According to Eq. (26) this implies that the A phonon peak in the clean limit has no Fano asymmetry ($|q_A| = \infty$), and the bare phonon peak intensity W_A (33) coincides with the integrated area ($W_A = W_A'$) [see Eq. (32)]. From Eq. (33) we get

$$W_A = \frac{\pi A^2}{\omega_A V^{3D}}\xi'^2(\omega_A) = \lambda\sigma_0\frac{\gamma_1^2}{\hbar\omega_A}\xi'^2(\omega_A), \qquad (45)$$

where $\sigma_0 = e^2/4\hbar d \approx 1816\ \Omega^{-1}$ cm^{-1} and $\lambda = (\sqrt{3}/\pi)g^2/(\hbar v/a)^2$ is the dimensionless phonon coupling which, using the value $g = 0.27$ eV estimated in Sec. II, results in $\lambda = 6 \times 10^{-3}$,[12] in agreement with the experimental estimates given in Refs. 5 and 13. Finally, we obtain that $\pi A^2/\omega_A V^{3D} = 4.35 \times 10^3\ \Omega^{-1}$ cm^{-2}.

To elucidate the doping dependence of the optical properties of the A mode, we show in Fig. 6 the quantities $\xi'(\omega_A)$, $\xi''(\omega_A)$ as functions of the charge doping n, along with the parameters W_A, W_A', P_A, and q_A. As mentioned above, due to the absence of 2–3 interband transitions, the imaginary part $\xi(\omega)$ is zero at $\omega = \omega_A$ in the clean limit $\eta = 0$ and relatively small for finite η [Fig. 6(b)], so that the spectral weight is dominated by the real part $\xi(\omega_A)$. In this context the small contribution at $\omega = \omega_A$ for finite η coming from the gapped 2–4 and 3–4 interband excitations gives rise to a finite Fano factor $|q_A| < \infty$ [Fig. 6(f)] but it does not affect sensibly the spectral weights W_A, W_A' and the spectral strength P_A. In particular, the doping dependence of these latter quantities, in the range n here considered, is dominated by the 3–4 interband transitions
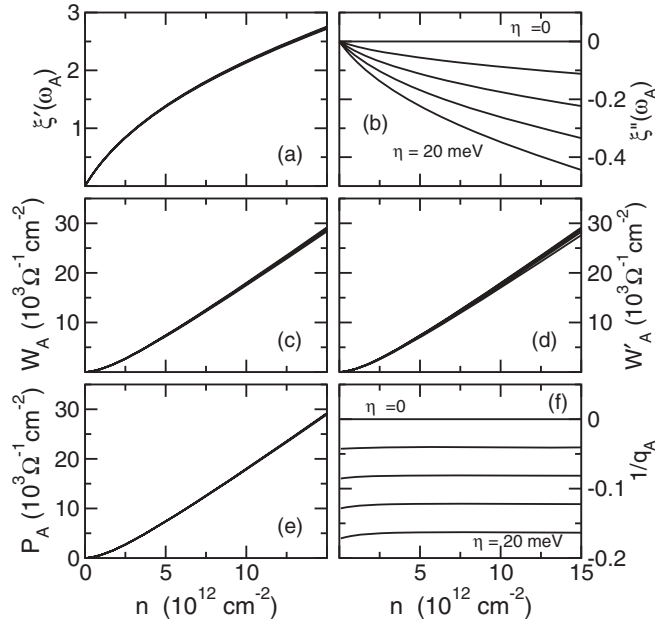
FIG. 6. Dimensionless quantities $\xi'(\omega_A)$, $\xi''(\omega_A)$, as well as the spectral weights W_A, W'_A, P_A, and the Fano factor q_A as functions of the charge concentration n for the clean limit ($\eta = 0$) and for finite damping $\eta = 5, 10, 15, 20$ meV. Curves for $\xi'(\omega_A)$, W_A, W'_A, P_A at zero and finite η are barely distinguishable.

[the third term in Eq. (43)], where $\xi'(\omega_A) \propto |\mu|$, so that, for $\xi''(\omega_A) \ll \xi'(\omega_A)$, $W_A = W'_A = P_A \propto [\xi'(\omega_A)]^2 \propto |\mu|^2 \approx n$.

Note also that, although the imaginary part $\xi''(\omega_A)$ does not contribute to the spectral weights W_A, W'_A, and P_A, it determines the magnitude of the Fano asymmetry factor, as shown in Fig. 6(f). As mentioned above, this is triggered by the finite spectral weight in $\xi''(\omega_A)$ due to the broadening η of the higher-energy transitions. Increasing the charge concentration n, and hence the chemical potential $|\mu|$, leads to an overall increase of $\xi''(\omega_A)$ and, since $\xi'(\omega_A)$ is related by the Kramers-Kronig relations to the low-energy part of $\xi''(\omega)$, to a similar increase of $\xi'(\omega_A)$. The charge-doping dependence of the magnitude of $\xi'(\omega_A)$ and $\xi''(\omega_A)$ is thus similar, making the Fano factor q_A almost independent of n. As we are going to see in the next section, the situation is different for the symmetric S mode, when its infrared activity is triggered by a finite-energy difference $\Delta \neq 0$.

V. FANO-RICE PROPERTIES IN GAPPED ($\Delta \neq 0$) BILAYER GRAPHENE

In the above section we have addressed the optical properties of the antisymmetric E_u mode in bilayer graphene in the absence of any electrostatic potential gradient Δ between the two layers. However, in most cases, the gating of the samples as well as the influence of the substrate give rise to a finite potential difference between the two layers. In this case, the antisymmetric A and symmetric S modes depicted in Fig. 1 are no more eigenvectors of the lattice dynamics although they still represent a suitable basis to investigate the optical properties of bilayer graphene. According to Eq. (21) we can distinguish three different channels responsible for the onset of phonon peaks in the infrared conductivity: the direct coupling of the

electron current with the A mode, which is already present for $\Delta = 0$ [first term of Eq. (21)]; the direct coupling with the S mode, which is induced by the presence of the gap Δ and vanishes for $\Delta \to 0$ [second term of Eq. (21)]; the mixed A-S mode optical coupling where the incoming light first excites the A lattice vibrations, which develop a S component due to the hybridized A-S phonon self-energy, and finally the light is re-emitted through the coupling of the A mode to the current [third term of Eq. (21)].

A. Undoped case $n = 0$, $\Delta \neq 0$

An interesting case to elucidate the role of the gap in triggering on the S-channel is the undoped case ($\mu = 0$) where the antisymmetric mode E_u is not involved [$\chi_{jA}^{\text{irr}}(\omega) = 0$],[35] and the only coupled lattice mode is the symmetric E_g one induced by the finite Δ. Such condition has been experimentally realized in Ref. 14. In Fig. 7(a) we show, for different values of Δ, the real and imaginary part of the dimensionless quantity $\xi_S(\omega) = \chi_{jS}(\omega)/A$, which rules the optical properties of the phonon resonance. An important difference here is that the low-energy interband transitions 2–3, that were forbidden in χ_{jA}, are allowed in the response function χ_{jS}. The imaginary part of $\xi_S(\omega)$ is thus finite at low energies (limited only by the opening of the optical gap $\tilde{\Delta}$) providing a finite Fano interference as long as $\omega_S \lesssim \tilde{\Delta}$. The sharp features in $\xi_S''(\omega)$ are reflected in peaked structures in the real part $\xi_S'(\omega)$. In particular, the structure at $\omega = 0.4$–0.5 eV can be associated with the transitions between bands 2 and 4, with lowest characteristic energy at $\approx \gamma_1 + \tilde{\Delta}/2$, whereas the structure at low energies $\omega = 0.05$–0.2 eV reflects the opening of the band gap on the transitions 2–3. It is worthwhile to note that, due to the mexican hat shape of the electronic dispersion, the lowest energy threshold is not determined by the gap Δ at the K point but by the actual optical gap $\tilde{\Delta} = \Delta \gamma_1 / \sqrt{\gamma_1^2 + \Delta^2}$ that lies at a finite momentum **k** at the bottom of the mexican hat [Fig. 7(b)]. The reduced dimensionality of the electronic dispersion in these points gives rise to a singular behavior in the density of states, which is reflected in a corresponding behavior in the particle-hole excitations in $\xi_S''(\omega)$. Such peaked structure in $\xi_S''(\omega)$ has important consequences also on the real part of $\xi_S(\omega)$, resulting in a strong peak at $\omega \approx \tilde{\Delta}$. When $\tilde{\Delta} \approx 0.2$ eV ($\Delta \approx 0.233$ eV) both $\xi_S'(\omega)$ and $\xi_S''(\omega)$ are peaked at $\omega \approx \omega_S$ and the phonon strength is expected to be strongly enhanced.

This trend, as well as the dependence on Δ of all the optical properties of the S phonon peak, is shown in Fig. 8. For $\tilde{\Delta} \lesssim \omega_S \approx 0.2$ eV the phonon strength P_S is increasing with Δ signalizing the switch on of the symmetric E_g mode. Such increase of the strength is mainly driven by $\xi''(\omega_S)$ while $\xi'(\omega_S) \approx 0$. This results in a *negative* peak where $W_S \approx 0$ and a negative integrate area $W'_S < 0$. The vanishing of $\xi'(\omega_S)$ results also in a Fano factor $q_S \approx 0$, which indeed corresponds to a negative symmetric shape.

B. Doped case $n \neq 0$, $\Delta \neq 0$

Unless using a double-gate device,[14] where the top and bottom gates are tuned to set the doping or the gap to zero, in single gated devices the gating induces at the same time as an inversion symmetry breaking and a finite doping. In this most
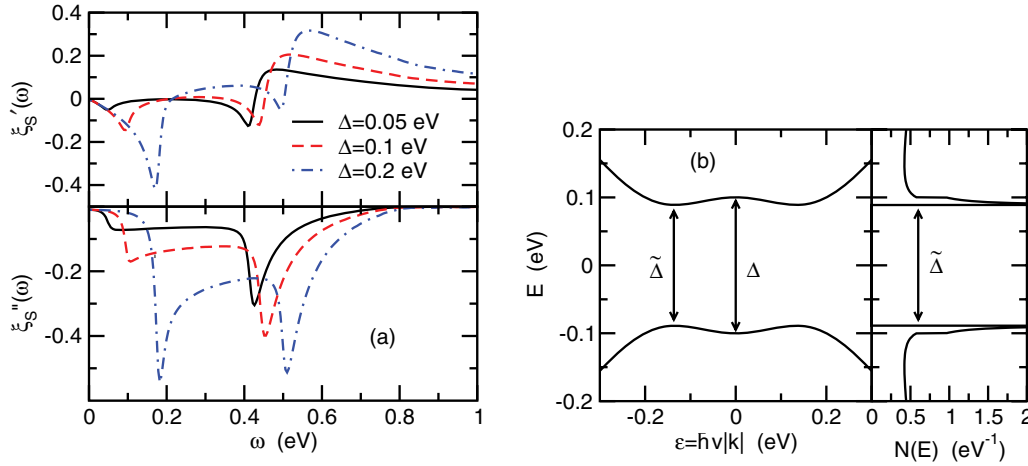
FIG. 7. (Color online) (a) Real part (upper panel) and imaginary part (lower panel) of the dimensionless response functions $\xi(\omega)$ for $\mu = 0$ and for different values of the gap: $\Delta = 0.05, 0.1, 0.2$ eV. Here we set $T = 10$ K and $\eta = 10$ meV. (b) Gapped dispersion (left panel) and corresponding density of states $N(\epsilon)$ (right panel) for $\Delta = 0.2$ eV. The vertical arrows mark the gap Δ at $\mathbf{k} = 0$ (K point) and the optical gap $\tilde{\Delta}$ at the bottom of the mexican hat. In this case the DOS presents a divergent behavior.

common case, both the E_u and E_g modes are simultaneously IR active. In order to investigate theoretically the optical properties of the phonon resonances, one has to employ the full Eq. (21), where both modes are present. The phonon spectral properties are then much more complex than in the $\Delta = 0$ case. Not only so we have different phonon channels contributing to the total features, but also the phonon propagator of each channel [e.g., the $D_{SS}(\omega)$ propagator], under particular conditions, can develop a double-pole structure, as discussed in Refs. 5, 23, 24, and 32 in the context of the Raman spectroscopy.

In general, we can attribute a different role to the several quantities appearing in Eq. (21). Here the mixed response functions $\chi_{j\nu}$ are mainly responsible for the magnitude and

the Fano line shape of the phonon features, while the pole structure of the phonon propagators $D_{\nu\nu'}$ is associated with the frequencies of the phonon resonances and to their linewidth. Keeping in mind this distinction, and since the frequency structure of $\chi_{j\nu}(\omega)$ varies over electronic energy scales while the phonon self-energy gives rise to a splitting of the S and A mode frequencies of a few cm^{-1}, we can in a very good approximation evaluate the functions $\chi_{j\nu}(\omega)$ at the bare phonon frequency $\omega \approx \omega_0$. In this context, the relevance of each phonon mode in the infrared spectroscopy is ruled by the characteristic phonon strength of the corresponding channel, i.e., $P_A = \pi |\chi_{jA}(\omega_0)|^2/\omega_0 V$ for the antisymmetric E_u mode, associated with the first term on the right-hand side (rhs) of Eq. (21), and $P_S = \pi |\chi_{jS}(\omega_0)|^2/\omega_0 V$ for the symmetric E_g mode, associated with the second term on the rhs of Eq. (21). It is also possible to define a mixed channel, related with the third term on the rhs of Eq. (21), characterized by a phonon strength $P_{AS} = \pi \sqrt{|\chi_{jA}(\omega_0)\chi_{S^\dagger j}(\omega_0)|}/\omega_0 V$. This channel is however quite weak in most cases,[19] and we neglect it in the following discussion.

The comparison of the phonon strengths associated with different A and S phonon modes is shown in Fig. 9, where we plot the relative intensity $R_{AS} = (P_A - P_S)/(P_A + P_S)$ as a function of the chemical potential μ (doping) and the band gap Δ induced by the vertical electric field. As discussed above, P_A is essentially driven by the doping, whereas P_S is induced by the gap Δ. According to the relative position in the μ vs Δ phase diagram, we can thus predict one mode to be dominant with respect to the other one. A "phonon switching,' namely the switch from the dominance of one phonon mode to another mode, is possible as a function of the gate voltage. In Fig. 9 we also show the location in the μ-Δ space of the experimental available data from Refs. 13 and 14. While the data of Ref. 14, in the double-gated device, were mainly collected along the neutral line $\mu = 0$, the optical conductivity measurements of Ref. 13 in the single-gate geometry span a much wider region, going from regions where the antisymmetric mode E_u is expected to dominate to regions where the optical features can be attributed mainly to the symmetric mode E_g. The actual
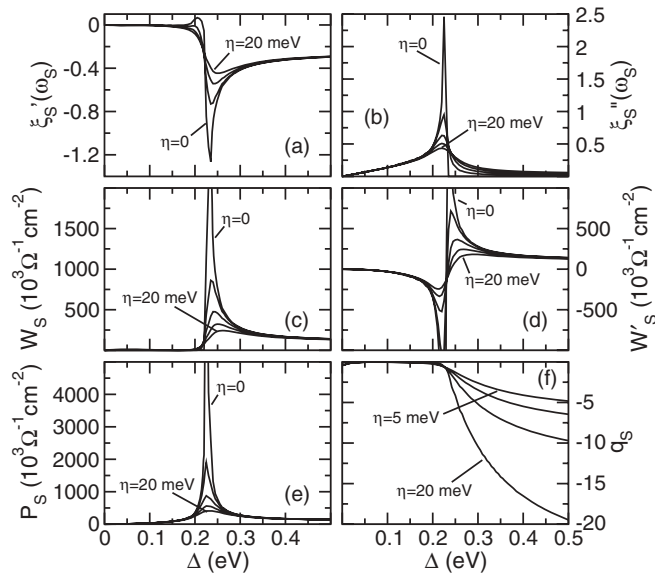

FIG. 8. Dimensionless quantities $\xi'(\omega_S)$, $\xi''(\omega_S)$, as well as the spectral weights W_S, W'_S, P_S, and the Fano factor q_S as functions of the gap Δ at $\mu = 0$ and for different values of the damping $\eta = 0, 5, 10, 15, 20$ meV.
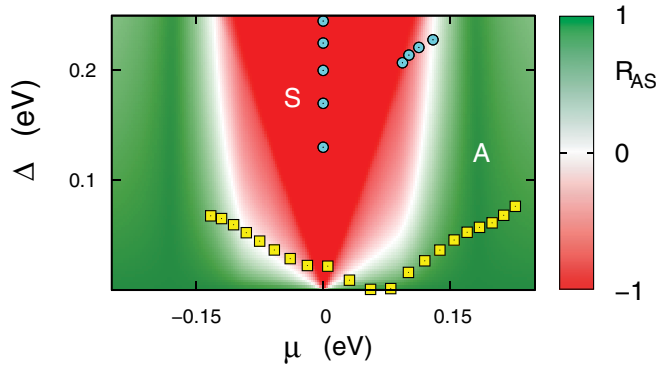
FIG. 9. (Color online) Phase diagram of the relative relevance of different phonon channels $R_{AS} = (P_A - P_S)/(P_A + P_S)$. In the green region optical features associated with the antisymmetric E_u mode are dominant, in the red one the dominant mode is the symmetric E_g one. Also shown here is the location in the μ-Δ space of the experimental available data [Refs. 13 (squares), 14 (circles)]. Adapted from Ref. 19.

evidence of such theoretically predicted phonon switching in the experimental data was discussed in Ref. 19, where we refer the reader for more details.

One should underline that the phonon switching is not directly related to the appearing of a double-peak structure in the optical conductivity, as observed in Raman spectroscopy.[5,23,24,32] What we are describing here is the dominant intensity of one phonon with respect to the other one, in other words, which phonon mode is most coupled to the light. This information is encoded in the mixed response function $\chi_{j\nu}$ which describes the coupling of the light with the mode ν. In this respect, as shown in Fig. 9, in bilayer graphene the two channels are to a good extent mutually exclusive. A different matter is the possibility, within a given phonon channel, to develop a two-peak phenomenology. This issue is related to the presence of a large off-diagonal phonon self-energy $\chi_{A,S}$ of the same order of the diagonal phonon self-energies $\chi_{A,A}$, $\chi_{S,S}$ in the 2×2 space of the phonon modes $\nu = A, S$. In this respect, since the phonon self-energy is a quantity which is shared in both Raman and IR spectroscopy, we expect that phonon features in optical conductivity can develop double-peak structures in the same regions where the Raman spectroscopy sees them. Things are however more complicated in the optical conductivity case since, as we show in Sec. VII, Raman spectroscopy in bilayer graphene is dominated only by the S channel. On the other hand, in the optical conductivity, we expect that the condition $\chi_{A,S} \neq 0$, ruling the double-peak features would arise in the same phase space where the mixed channel P_{AS} [second line in Eq. (21)] is of the order of P_A, P_S. In this situation spectral interferences between the different channels can occur making the scenario more complex than in Raman spectroscopy.

VI. FULL TIGHT-BINDING MODEL

The simplified model considering only the leading tight-binding terms γ_0 and γ_1 has some significant limitations. For example, within this model the intensity of the IR active E_u drops exactly to zero in the undoped limit $\mu \to 0$. The generalization of this model to bulk graphite would predict

thus no IR activity at all, despite the clear evidence of a phonon resonance reported already in the 1970s.[36,37] As a matter of fact, the evidence of such phonon intensity in graphite was reconciled with the charged-phonon theory in Ref. 21 where it was shown that the inclusion of higher-order tight-binding terms, in particular of the ones breaking the particle-hole symmetry, is responsible for the observed phonon activity. It is thus interesting to investigate to which extent these higher-order tight-binding terms can affect the results for the bilayer graphene.

We address this issue by including explicitly in the Hamiltonian of bilayer graphene the higher-order tight-binding hoppings γ_3, γ_4 as well as the crystal field δ which differentiate the atoms B1, A2 from the atoms A1, B2. Close to the K point, we can write

$$\hat{H}_{\mathbf{k}} = \begin{pmatrix} \Delta/2 & v\pi_- & v_4\pi_- & v_3\pi_+ \\ v\pi_+ & \delta + \Delta/2 & \gamma_1 & v_4\pi_- \\ v_4\pi_+ & \gamma_1 & \delta - \Delta/2 & v\pi_- \\ v_3\pi_- & v_4\pi_+ & v\pi_+ & -\Delta/2 \end{pmatrix}, \quad (46)$$

where $v_i = \gamma_i/\gamma_0$. We consider here typical values of $\gamma_3 = 0.29$ eV, $\gamma_4 = -0.13$ eV, and $\delta = 0.022$ eV.[38] We evaluate consequently also the current operator

$$\hat{j}_{\mathbf{k},y} = -\frac{e}{\hbar}\frac{d}{dk_y}\hat{H}_{\mathbf{k}}$$

$$= -ev\hat{I}(\hat{\sigma}_y) - ev_4\hat{\sigma}_y(\hat{I}) + ev_3\frac{\hat{\sigma}_x(\hat{\sigma}_y) + \hat{\sigma}_y(\hat{\sigma}_x)}{2}, \quad (47)$$

and the electron-phonon scattering matrices

$$\hat{V}_A = ig\hat{\sigma}_z(\hat{\sigma}_x) + ig_4\hat{\sigma}_x(\hat{\sigma}_z), \quad (48)$$

$$\hat{V}_S = ig\hat{I}(\hat{\sigma}_x) - ig_3\frac{\hat{\sigma}_x(\hat{\sigma}_x) - \hat{\sigma}_y(\hat{\sigma}_y)}{2}. \quad (49)$$

The terms g_3, g_4 represent the electron-phonon coupling associated respectively with the hopping terms γ_3 and γ_4 and they can be related to the corresponding deformation potentials which have been recently evaluated by DFT calculations.[39] We get namely $g_3 = 0.033$ eV and $g_4 = 0.018$ eV.

As two representative limits, we show in Figs. 10(a) and 10(b) the phonon strength P_A and the Fano parameter q_A for the E_u mode in the ungapped case as functions of the doping n, and in Figs. 10(c) and 10(d) the phonon strength P_S and the Fano parameter q_S for the E_g mode in the undoped case as functions of the electric field parametrized by the gap Δ at the K point. As found for bulk graphite in Ref. 21, a finite phonon strength $P_A \approx 0.62 \times 10^3$ Ω^{-1} cm^{-2} [weakly visible on the scale of Fig. 10(a)] is now triggered by the higher-order tight-binding terms at the neutral point. However, apart from a slight asymmetry for electron and hole doping, the inclusion of such tight-binding terms does not change qualitatively the results at finite doping, with a roughly linear increasing of the phonon strength P_A as function of $|n|$. In addition, such residual phonon strength P_A at the neutrality point is easily overwhelmed in gated systems by the presence of the symmetric E_g mode with $P_S \gg P_A$ [Fig. 10(c)]. The Δ dependence of the optical properties of such mode (phonon strength P_S, Fano parameter q_S) is also barely affected by the presence of the higher-order tight-binding terms, so that we can conclude that the scenario presented in Secs. IV and V is
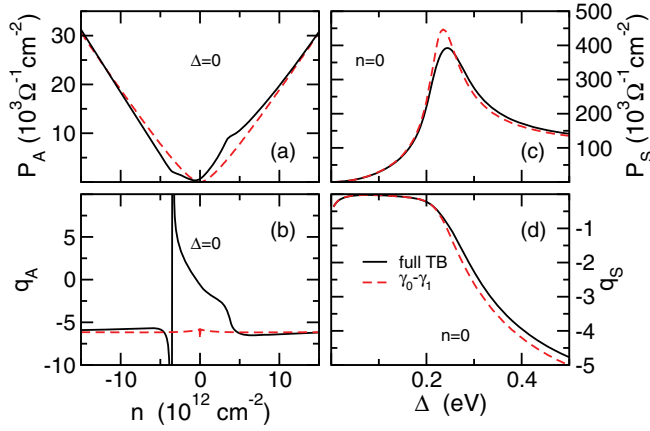
FIG. 10. (Color online) Phonon strength P_A (a) and Fano parameter q_A (b) for the E_u mode as functions of doping n for $\Delta = 0$ including all the relevant tight-binding parameters (black solid line) and using the simple γ_0-γ_1 model of Sec. IV (red dashed line), with $T = 10$ K and $\eta = 20$ meV. (c),(d) Same quantities P_S, q_S for the E_g mode at $n = 0$ as functions of the gap Δ.

generally robust in realistic materials against the inclusion of higher-order tight-binding terms, except in the case of ungated and undoped bilayer graphene, as it could be relevant in suspended samples.

VII. CHARGED PHONON THEORY FOR THE RAMAN RESPONSE

In the previous sections we have outlined in detail how a quantitative implementation of the charged-phonon theory gives rise in the infrared optical spectroscopy of bilayer graphene to a phonon intensity and to an asymmetric Fano-like shape for the A mode as well as for the S mode once this latter is turned on by the interlayer potential. In particular, such analysis shows that for gate potential V_g close to the charged neutrality point, the negative phonon peak can been attributed to the S mode with a phonon activity strongly dependent on the gate voltage V_g and with a strong Fano character with $q_S \approx 0$, induced by the interference with the low-energy 2–3 interband particle-hole excitations.

One can wonder why the same S mode, under the same conditions (namely tuning charge concentration and band gap Δ), does not present in the Raman response any significant Fano asymmetry and strong dependence of the phonon intensity upon V_g.[6,7,9] In this section we show that this different behavior for the infrared and Raman spectroscopy can be naturally explained within the context of the charged-phonon theory.

In our analysis we focus on the possible changes in the Raman features of the phonon resonances at $\sim$1590 cm^{-1} as functions the charge doping and the band gap, i.e., quantities that typically affect only the low-energy excitations close to the Fermi level. We do not address the possible dependence of the phonon intensity on the external laser energy.[40,41] We also assume a relatively small gate-induced doping, so that the chemical potential is much less than the laser energy, in a region where the absolute Raman intensity of the phonon peak at $\sim$1590 cm^{-1} is constant.[10] Within this context, we employ the effective-mass approximation,[42] when the only relevant

quantity is the Raman shift $\omega = \omega_{in} - \omega_{out}$, of the order of the phonon energy, $\omega \approx \omega_0$. References 40 and 41 showed also how the main electronic transitions responsible for the phonon intensity were associated with high-energy processes, of the order of the laser energy $\omega_{in} \approx 1$ eV or of the order of the π bandwidth $W \approx 6$–7 eV, in any case much larger than the phonon energy scale. As we shall see, we will recover this result in our simplified scheme and we will show how it can explain the different phenomenology of Raman spectroscopy with respect to the infrared spectroscopy. For simplicity we consider unpolarized isotropic Raman scattering. The Raman intensity $I(\omega)$ can be related to the imaginary part of the Raman response function,[42] namely

$$I(\omega) = -\frac{1}{\pi}[1 + b(\omega/T)]\mathrm{Im}\chi_{RM}(\omega), \quad (50)$$

where $b(x) = 1/[\exp(x) - 1]$ is the Bose-Einstein function and $\chi_{RM}(\omega)$ is the analytical continuation to the real frequency axis of the Raman response function $\chi_{RM}(i\omega_m)$, whose explicit definition and derivation are given in Appendix B. Just as in the case of the optical conductivity, the irreducible part of $\chi_{RM}(\omega)$ provides the electronic Raman background, which is proportional to the current-current response function involved in the optical conductivity. In a similar way, within the charged-phonon theory, the bubble diagrams mediated by a phonon propagator, as in Fig. 2(b), are associated with the onset of the phonon peaks in the Raman response. In particular, we can write, for $\Delta \neq 0$,

$$
\begin{aligned}
\Delta\chi_{RM}(\omega) = {} & \chi_{\gamma S}(\omega)D_{SS}(\omega)\chi_{S^\dagger\gamma}(\omega) \\
& + \chi_{\gamma A}(\omega)D_{AA}(\omega)\chi_{A^\dagger\gamma}(\omega) \\
& + [\chi_{\gamma S}(\omega)D_{SA}(\omega)\chi_{A^\dagger\gamma}(\omega) + \mathrm{H.c.}], \quad (51)
\end{aligned}
$$

where $\chi_{\gamma\nu}(\omega)$ are Raman mixed response functions involving one Raman vertex γ, described by the effective-mass approximation, and one electron-phonon scattering operator. Explicit expressions for the Raman vertices for different polarizations are given in Appendix B. It is worthwhile to point out that close to the K point the Raman vertex scattering operator for the xx polarization involved in Eq. (51) reads

$$\hat{\gamma}_{\mathbf{k}}^{xx} \propto \hat{I}(\hat{\sigma}_x) \propto i\hat{V}_S. \quad (52)$$

This observation permits us to relate the Raman spectroscopy in the effective-mass approximation to the response functions previously discussed. In particular, using the relation (52), we can relate the Raman mixed response functions to the phonon self-energy. We obtain for instance $\chi_{\gamma S}(\omega) \propto \chi_{SS}(\omega)$ and $\chi_{\gamma A}(\omega) \propto \chi_{SA}(\omega)$. Just as in the infrared response, also in this case the Raman spectral strength of each mode will be $P_\nu^{Raman} \propto |\chi_{\gamma\nu}(\omega_\nu)|^2$ and the Fano asymmetry factor $q_\nu^{Raman} = -\chi'_{\gamma\nu}(\omega_\nu)/\chi''_{\gamma\nu}(\omega_\nu)$.

A crucial difference with respect to the infrared spectroscopy is the different dependence of the Raman mixed response functions $\chi_{\gamma\nu}$ on the high-energy interband transitions when compared to the infrared response functions $\chi_{j\nu}$. One should keep in mind that the linear Dirac-like dispersion $\epsilon = \hbar v|\mathbf{k}|$ of the single-layer graphene extends only up to 3–5 eV. However, as we saw in Sec. IV, in the clean limit and in the absence of the gap Δ the imaginary part of $\chi_{jA}(\omega)$, and hence also the real part due to the Kramers-Kronig relations,

are uniquely determined by low-energy interband transitions $\gamma \leqslant |\omega| \leqslant \gamma + 2|\mu|$, so that the high-energy cutoff E_c does not play any role. One can see that such results hold true also for $\chi_{jS}(\omega)$ and for generic finite η and Δ, in a sense that that the imaginary part of the infrared mixed response functions $\chi_{j\nu}(\omega)$ is not divergent for $\omega \to \infty$ so that the high-energy cutoff E_c can be safely set to infinity.

The situation is different when the Raman response function is considered. In this case, using Eq. (52), we get $\chi_{\gamma S} \propto \chi_{SS}$ and $\chi_{\gamma A} \propto \chi_{SA}$. The function $\chi_{SS}(\omega)$, which corresponds to the phonon self-energy for the symmetric E_g mode, has been widely analyzed in the literature.[12,23,24] In particular, its imaginary part increases linearly at high energy, $\chi''_{SS}(\omega) \sim \omega$. As a consequence, from the Kramers-Kronig relations, the magnitude of the real part of $\chi_{SS}(\omega)$ is dominated by the high-energy processes, i.e., by high-energy cutoff E_c, $\chi'_{SS}(\omega) \sim E_c$. On a physical ground, this cutoff E_c can be identified with the π bandwidth W or with the highest energy ω_{in} above which the effective-mass approximation breaks down.

From a careful inspection, one can see that both the real and imaginary parts of almost all the mixed response functions $\chi_{\gamma,\nu}$ are only weakly dependent on the high-energy cutoff E_c. The only exception is the real part of the Raman coupling with the S mode, $\text{Re}\chi_{\gamma,S}$, which scales with E_c. Since this is the highest energy scale involved in the system, we have $\chi'_{\gamma S} \gg \chi''_{\gamma S}, \chi'_{\gamma A}, \chi''_{\gamma A}$. As a consequence we see that the phonon Raman spectroscopy is dominated by direct coupling of the Raman scattering operator with the E_g symmetric mode [first line of Eq. (51)], whereas other channels involving the E_u are marginal, independent of the charge doping level or of the interlayer potential difference Δ. Other interesting consequences: (i) since $\chi'_{\gamma S} \gg \chi''_{\gamma S}$, the Fano factor for the dominant S channel results in $|q_S^{\text{Raman}}| = |\chi'_{\gamma S}(\omega_S)/\chi''_{\gamma S}(\omega_S)| \gg 1$ and the Raman phonon peaks are expected to be positive and symmetric, in agreement with the experiments; (ii) the magnitude of the Raman phonon strength $P_S^{\text{Raman}} \propto [\chi'_{\gamma S}]^2$ is mainly dominated by the energy cutoff E_c, so that it does not depend significantly on the low-energy features related to the charge doping or to the opening of the gap Δ, also in agreement with the experimental observations.

Note that the fact that the phonon Raman response is dominated by the direct coupling of polarizability to the S mode does not exclude that a double-peak structure could be observed. Indeed, as we saw in Sec. V, under suitable conditions the phonon propagator $D_{SS}(\omega)$ itself, as well as $D_{AA}(\omega)$, can develop a double-peak structure as a consequence of the phonon-modes hybridization triggered by the mixed phonon self-energy χ_{AS}.[5,23,24,32]

VIII. CONCLUSIONS

In this paper we have provided a comprehensive derivation of the charged-phonon theory applied to investigate the optical properties of the phonon peaks in the optical conductivity of bilayer graphene. The origin of the phonon activity and its relation with the occurrence of a Fano effect have been elucidated. The dependence of these properties on the tunable microscopical parameters, i.e., the doping and the band gap induced by an external gate voltage, has been discussed in detail. We have also compared the charged-phonon theory

in the infrared and Raman spectroscopy, accounting for the different phenomenology of the phonon peaks in these two different optical probes.

The theory presented here provides a suitable tool to characterize quantitatively bilayer graphene in terms of the intensity and Fano asymmetry of the infrared phonon peaks. Further future developments of the present analysis could investigate the dependence of the phonon optical properties on the different symmetry breakings,[43–50] in order to provide a fingerprint for the possible underlying instabilities. The microscopical characterization of the phonon optical properties also sheds light on the underlying physics of the electron-phonon interaction. While the present work was focused on bilayer graphene, as the simplest graphitic system with infrared-active modes, the theory presented here can be generalized in a straightforward way to multilayer graphene[22] and to bulk graphite.[21]

The general scheme discussed in this work to investigate within a microscopic many-body approach the Fano effect can be applied, with the due modifications, also to different classes of materials. One remarkable example is provided by layered systems with different atomic species in the units cell, for instance MoS_2, Bi_2Se_3, where phonon anomalies have been detected in infrared and Raman spectroscopy.[51,52] A second interesting case is the As phonon mode in the pnictide $Ba(Fe_{1-x}Co_x)_2As_2$, which displays a concomitant presence of intensity variation and asymmetry as a function of doping and/or temperature, in particular across the magnetostructural transition.[53] In all these cases the understanding of the phonon anomalies can shed new light on the underlying bulk electronic structure. In this sense phonon spectroscopy can represent a powerful and alternative tool to investigate electronic excitations also in correlated materials, provided that a correct implementation of the Fano-Rice theory is used to relate the phonon and electronic response, taking into account the microscopic selection rules.

APPENDIX A: ANALYTICAL RESULTS FOR THE CHARGED-PHONON THEORY OF IR RESPONSE IN UNGAPPED BILAYER GRAPHENE

In this appendix we provide the analytical derivation of the optical properties of the A mode in the absence of electrostatic bias between the layers, $\Delta = 0$. To this aim it is convenient, for the simple tight-binding model with γ_0-γ_1 considered, and in the linear expansion close to the K point, to employ the cylindric coordinates, where the Hamiltonian reads

$$\hat{H}_{\mathbf{k}} = \begin{pmatrix} \Delta/2 & \epsilon_k^- & 0 & 0 \\ \epsilon_k^+ & \Delta/2 & \gamma_1 & 0 \\ 0 & \gamma_1 & -\Delta/2 & \epsilon_k^- \\ 0 & 0 & \epsilon_k^+ & -\Delta/2 \end{pmatrix}, \quad \text{(A1)}$$

where $\epsilon_k^{\pm} = \epsilon_k e^{\pm i\theta_k} \epsilon = \hbar v|k|$, and $\theta_k = \arctan(k_y/k_x)$.

The Hamiltonian is diagonalized by the transformation

$$\tilde{\hat{H}}_k = \hat{M}_{\mathbf{k}}^{-1} \hat{H}_{\mathbf{k}} \hat{M}_{\mathbf{k}} = \hat{E}_k, \tag{A2}$$

where

$$\hat{E}_k = \begin{pmatrix} E_{1k} & 0 & 0 & 0 \\ 0 & E_{2k} & 0 & 0 \\ 0 & 0 & E_{3k} & 0 \\ 0 & 0 & 0 & E_{4k} \end{pmatrix} \tag{A3}$$

[band labels according Fig. 1(b)],

$$\hat{M}_{\mathbf{k}} = \hat{R}_{\theta_k}^{-1} \hat{F}_k, \tag{A4}$$

$$\hat{R}_\theta = \begin{pmatrix} e^{i\theta_k} & 0 & 0 & 0 \\ 0 & 1 & 0 & 0 \\ 0 & 0 & 1 & 0 \\ 0 & 0 & 0 & e^{-i\theta_k} \end{pmatrix}, \tag{A5}$$

$$\hat{F}_k = \frac{1}{\sqrt{2}} \begin{pmatrix} -s_k & -c_k & c_k & s_k \\ c_k & s_k & s_k & c_k \\ -c_k & s_k & -s_k & c_k \\ s_k & -c_k & -c_k & s_k \end{pmatrix}. \tag{A6}$$

Here

$$s_k = \frac{1}{\sqrt{2}} \sqrt{1 - \frac{\gamma_1}{2\sqrt{\gamma_1^2/4 + \epsilon_k^2}}}, \tag{A7}$$

$$c_k = \frac{1}{\sqrt{2}} \sqrt{1 + \frac{\gamma_1}{2\sqrt{\gamma_1^2/4 + \epsilon_k^2}}}, \tag{A8}$$

so that

$$2 s_k c_k = \frac{|\epsilon_k|}{\sqrt{\gamma_1^2/4 + \epsilon_k^2}}. \tag{A9}$$

In the diagonalized basis we have

$$\tilde{\hat{j}}_{\mathbf{k},y} = \hat{M}_{\mathbf{k}}^{-1} \hat{j}_{\mathbf{k},y} \hat{M}_{\mathbf{k}}$$
$$= -ev \begin{pmatrix} -S_k s_\theta & -i C_k c_\theta & C_k s_\theta & i S_k c_\theta \\ i C_k c_\theta & -S_k s_\theta & i S_k c_\theta & -C_k s_\theta \\ C_k s_\theta & -i S_k c_\theta & S_k s_\theta & -i C_k c_\theta \\ -i S_k c_\theta & -C_k s_\theta & i C_k c_\theta & S_k s_\theta \end{pmatrix}, \tag{A10}$$

where $S_k = 2 s_k c_k$, $C_k = c_k^2 - s_k^2$, $s_\theta = \sin\theta$, $c_\theta = \cos\theta$.

In a similar way we obtain

$$\tilde{\hat{V}}_{\mathbf{k},A} = ig \begin{pmatrix} 0 & -c_\theta & -i s_\theta & 0 \\ -c_\theta & 0 & 0 & -i s_\theta \\ i s_\theta & 0 & 0 & c_\theta \\ 0 & i s_\theta & c_\theta & 0 \end{pmatrix}, \tag{A11}$$

$$\tilde{\hat{V}}_{\mathbf{k},S} = ig \begin{pmatrix} -S_k c_\theta & i C_k s_\theta & C_k c_\theta & -i S_k s_\theta \\ -i C_k s_\theta & -S_k c_\theta & -i S_k s_\theta & -C_k c_\theta \\ C_k c_\theta & i S_k s_\theta & S_k c_\theta & i C_k s_\theta \\ i S_k s_\theta & -C_k c_\theta & -i C_k s_\theta & S_k c_\theta \end{pmatrix}. \tag{A12}$$

Note that the interband transitions between bands 1–4 and 2–3 are missing in the electron-phonon matrix (A11) for the A

mode, so that these interband transitions will not be operative in any response function involving such electron-phonon coupling, like for instance the mixed response function for the infrared activity as well as the phonon self-energy.

The mixed response function reads in the diagonalized basis as

$$\chi_{jv}(i\omega_m) = N_s N_v \frac{T}{N} \sum_{\mathbf{k},n} \text{Tr}[\tilde{\hat{j}}_{\mathbf{k},y} \hat{g}(k, i\omega_n + i\omega_m)$$
$$\times \tilde{\hat{V}}_{\mathbf{k},v} \hat{g}(k, i\omega_n)], \tag{A13}$$

where $\hat{g}(k, i\omega_n) = 1/[(i\hbar\omega_n + \mu)\hat{I} - \tilde{\hat{H}}_k]$, is the electronic Green's function in the diagonalized basis.

Using now Eqs. (A3), (A10), (A11), (A12), we can easily obtain

$$\chi_{jv}(i\omega_m) = \frac{1}{N} \sum_{\mathbf{k},\alpha,\beta} C_{jv,\mathbf{k}}^{\alpha\beta} \Pi_k^{\alpha\beta}(i\omega_m), \tag{A14}$$

where

$$C_{jv,\mathbf{k}}^{\alpha\beta} = N_s N_v (\tilde{\hat{j}}_{\mathbf{k},y})_{\alpha\beta} (\tilde{\hat{V}}_{\mathbf{k},v})_{\beta\alpha}, \tag{A15}$$

and

$$\Pi_k^{\alpha\beta}(i\omega_m) = \frac{f(E_{k,\alpha} - \mu) - f(E_{k,\beta} - \mu)}{E_{k,\alpha} - E_{k,\beta} + \hbar i\omega_m}. \tag{A16}$$

Note that the function $\pi_k^{\alpha\beta}(i\omega_m)$ does not depend, in cylindrical coordinates, on the angle θ_k but only on the momentum modulus $k = |\mathbf{k}|$. Writing $\sum_{\mathbf{k}} = \int 2\pi k\, dk \int d\theta_k / 2\pi$, the quantity $C_{jv,\mathbf{k}}^{\alpha\beta}$ can be replaced thus with its average over the angle θ_k, $C_{jv,\mathbf{k}}^{\alpha\beta} \to C_{jv,k}^{\alpha\beta} = \langle C_{jv,\mathbf{k}}^{\alpha\beta} \rangle_{\theta_k}$. Using (A11), (A12), it is now easy to see that $C_{jS,k}^{\alpha\beta}$ averages out, whereas $|C_{jA,k}^{\alpha\beta}| = gevN_s N_v \gamma_1 / 4\sqrt{(\hbar vk)^2 + \gamma_1^2}$, which recovers Eq. (41). The relative change of sign between different interband contributions stems from $(\tilde{\hat{j}}_{\mathbf{k},y})_{\alpha\beta}(\tilde{\hat{V}}_{\mathbf{k},v})_{\beta\alpha} = -(\tilde{\hat{j}}_{\mathbf{k},y})_{\beta\alpha}(\tilde{\hat{V}}_{\mathbf{k},v})_{\alpha\beta}$.

APPENDIX B: CHARGED-PHONON THEORY FOR RAMAN SPECTROSCOPY

In this appendix we provide a brief derivation of the charged-phonon theory as applied to the case of Raman spectroscopy within the effective-mass approximation. To this end it is useful to recall the tight-binding Hamiltonian which can be written as

$$\hat{H}_{\mathbf{p}} = \begin{pmatrix} \Delta/2 & \gamma_0 f_{\mathbf{p}}^* & 0 & 0 \\ \gamma_0 f_{\mathbf{p}} & \Delta/2 & \gamma_1 & 0 \\ 0 & \gamma_1 & -\Delta/2 & \gamma_0 f_{\mathbf{p}}^* \\ 0 & 0 & \gamma_0 f_{\mathbf{p}} & -\Delta/2 \end{pmatrix}, \tag{B1}$$

where

$$f_{\mathbf{p}} = e^{-i p_x a/\sqrt{3}} + 2 e^{i p_x a/2\sqrt{3}} \cos(p_y a/2). \tag{B2}$$

Close to the $K = (4\pi/3a, 0)$ point we can write $\mathbf{p} = K + \mathbf{k}$, and by expanding for small $\mathbf{k}$ we obtain (7). The Raman vertex $\hat{\gamma}(\phi, \phi')$ for a particular polarization geometry can be now

defined as $\gamma(\phi,\phi') = (1/N)\sum_{\mathbf{k},\sigma} \Psi_{\mathbf{k},\sigma}^{\dagger} \hat{\gamma}_{\mathbf{k}}(\phi,\phi')\Psi_{\mathbf{k},\sigma}$ where

$$
\begin{aligned}
\hat{\gamma}_{\mathbf{k}} &= (\mathbf{e}_i \cdot \nabla_{\mathbf{k}})(\mathbf{e}_o \cdot \nabla_{\mathbf{k}})\hat{H}_{\mathbf{k}} \\
&= \cos\phi \cos\phi' \hat{\gamma}_{\mathbf{k}}^{xx} + \sin\phi \sin\phi' \hat{\gamma}_{\mathbf{k}}^{yy} \\
&\quad + \cos\phi \sin\phi' \hat{\gamma}_{\mathbf{k}}^{yx} + \cos\phi \sin\phi' \hat{\gamma}_{\mathbf{k}}^{xy},
\end{aligned}
\tag{B3}
$$

where $\mathbf{e}_i = (\cos\phi, \sin\phi)$ and $\mathbf{e}_o = (\cos\phi', \sin\phi')$ are the directions of the *incoming* and *outcoming* photon, respectively, and $\hat{\gamma}_{\mathbf{k}}^{ij} = \partial^2 \hat{H}_{\mathbf{k}}/\partial k_i \partial k_j$. Using Eq. (B1) we obtain, close to the K point,

$$
\hat{\gamma}_{\mathbf{k}}^{xx}(K) = -\hat{\gamma}_{\mathbf{k}}^{yy}(K) = \hat{I}(\hat{\sigma}_x)/4a^2,
\tag{B4}
$$

$$
\hat{\gamma}_{\mathbf{k}}^{xy}(K) = \hat{\gamma}_{\mathbf{k}}^{yx}(K) = -\hat{I}(\hat{\sigma}_y)/4a^2,
\tag{B5}
$$

while, at the K' point,

$$
\hat{\gamma}_{\mathbf{k}}^{xx}(K') = -\hat{\gamma}_{\mathbf{k}}^{yy}(K') = \hat{I}(\hat{\sigma}_x)/4a^2,
\tag{B6}
$$

$$
\hat{\gamma}_{\mathbf{k}}^{xy}(K') = \hat{\gamma}_{\mathbf{k}}^{yx}(K') = \hat{I}(\hat{\sigma}_y)/4a^2.
\tag{B7}
$$

We can write the Raman (RM) response function in the Matsubara imaginary time for generic polarization as

$$
\chi_{\mathrm{RM}}(\tau,\phi,\phi') = -\langle T_\tau \gamma(\tau,\phi,\phi')\gamma(\phi,\phi')\rangle.
\tag{B8}
$$

For unpolarized Raman scattering we have to average over ϕ and ϕ', $\chi_{\mathrm{RM}}(i\omega_m) = \int d\phi/(2\pi)d\phi'/(2\pi)\chi_{\mathrm{RM}}(i\omega_m,\phi,\phi')$. We get then

$$
\begin{aligned}
\chi_{\mathrm{RM}}(i\omega_m) &= \chi_{\gamma^{xx}\gamma^{xx}}(i\omega_m) + \chi_{\gamma^{yy}\gamma^{yy}}(i\omega_m) \\
&\quad + \chi_{\gamma^{xy}\gamma^{xy}}(i\omega_m) + \chi_{\gamma^{yx}\gamma^{yx}}(i\omega_m) \\
&= \sum_{i=x,y} \chi_{\gamma^{ii}\gamma^{ii}}(i\omega_m) + \sum_{i=x,y} \chi_{\gamma^{i\bar{i}}\gamma^{i\bar{i}}}(i\omega_m),
\end{aligned}
\tag{B9}
$$

where we used the shorthand notation $\bar{x} = y$, $\bar{y} = x$.

For the electronic Raman scattering, taking also in account the different K and K' points, these four contributions are

degenerate and we get on the real frequency axis

$$
\chi_{\mathrm{RM}}(\omega) = 4\chi_{\gamma^{xx}\gamma^{xx}}(\omega).
\tag{B10}
$$

Note that, since $\hat{\gamma}_{\mathbf{k}}^{xx} \propto \hat{I}(\hat{\sigma}_x) \propto \hat{j}_{\mathbf{k},x}$, this result explicitly shows also that the electronic Raman background is directly related to the electronic optical conductivity.

Let us focus now on the onset of phononic peaks within the framework of the Fano-Rice theory. For a generic case, for finite charge concentration n and finite gap Δ, we can write

$$
\begin{aligned}
\Delta\chi_{\mathrm{RM}}(\omega) &= \sum_{i=x,y}\sum_{\nu\nu'} \chi_{\gamma^{ii}\nu}(\omega)D_{\nu\nu'}(\omega)\chi_{\nu'\gamma^{ii}}(\omega) \\
&\quad + \sum_{i=x,y} \chi_{\gamma^{i\bar{i}}\nu}(\omega)D_{\nu\nu'}(\omega)\chi_{\nu'\gamma^{i\bar{i}}}(\omega),
\end{aligned}
\tag{B11}
$$

where the label ν specifies at the same time the A vs S phonon branch and the x vs y direction of the lattice displacement. The notation $\bar{i}$ denotes in addition $\bar{i} = y$ if $i = x$ and $\bar{i} = x$ if $i = y$.

Expanding explicitly the sums over i, $\bar{i}$, ν, and ν' in Eq. (B11), as well as the summation over the different K and K' points of the Brillouin zone, and taking into account the degeneracies $\hat{\gamma}_{\mathbf{k}}^{xx} = -\hat{\gamma}_{\mathbf{k}}^{yy}$, $\hat{\gamma}_{\mathbf{k}}^{xy} = \hat{\gamma}_{\mathbf{k}}^{yx}$, $D_{S_xS_x} = D_{S_yS_y}$, $D_{A_xA_x} = D_{A_yA_y}$, $D_{A_xS_x} = D_{A_yS_y}$, $D_{S_xA_x} = D_{S_yA_y}$, after a few straightforward steps, we end up with

$$
\begin{aligned}
\Delta\chi_{\mathrm{RM}}(\omega) &= \chi_{\gamma S}(\omega)D_{SS}(\omega)\chi_{S^{\dagger}\gamma}(\omega) \\
&\quad + \chi_{\gamma A}(\omega)D_{AA}(\omega)\chi_{A^{\dagger}\gamma}(\omega) \\
&\quad + \chi_{\gamma S}(\omega)D_{SA}(\omega)\chi_{A^{\dagger}\gamma}(\omega) \\
&\quad + \chi_{\gamma A}(\omega)D_{AS}(\omega)\chi_{S^{\dagger}\gamma}(\omega),
\end{aligned}
\tag{B12}
$$

where, due to the degeneracies of the systems, the Raman vertex operators and the electron-phonon vertex operators have been chosen for simplicity in Eq. (B12) as $\gamma \equiv \gamma^{xx}$, $S = S_x$, $A = A_x$.

[1] A. C. Ferrari, J. C. Meyer, V. Scardaci, C. Casiraghi, M. Lazzeri, F. Mauri, S. Piscanec, D. Jiang, K. S. Novoselov, S. Roth, and A. K. Geim, Phys. Rev. Lett. **97**, 187401 (2006).

[2] J. Yan, Y. Zhang, P. Kim, and A. Pinczuk, Phys. Rev. Lett. **98**, 166802 (2007).

[3] S. Pisana, M. Lazzeri, C. Casiraghi, K. S. Novoselov, A. K. Geim, A. C. Ferrari, and F. Mauri, Nat. Mater. **6**, 198 (2007).

[4] A. Das, S. Pisana, B. Chakraborty, S. Piscanec, S. K. Saha, U. V. Waghmare, K. S. Novoselov, H. R. Krishnamurty, A. K. Geim, A. C. Ferrarri, and A. K. Sood, Nat. Nanotech. **3**, 210 (2008).

[5] L. M. Malard, D. C. Elias, E. S. Alves, and M. A. Pimenta, Phys. Rev. Lett. **101**, 257401 (2008).

[6] J. Yan, E. A. Henriksen, P. Kim, and A. Pinczuk, Phys. Rev. Lett. **101**, 136804 (2008).

[7] D. M. Basko, S. Piscanec, and A. C. Ferrari, Phys. Rev. B **80**, 165413 (2009).

[8] I. Calizo, I. Bejenari, M. Rahman, G. Liu, and A. A. Baladin, J. Appl. Phys. **106**, 043509 (2009).

[9] C. Casiraghi, Phys. Rev. B **80**, 233407 (2009).

[10] C.-F. Chen, C.-H. Park, B. W. Boudouris, J. Horng, B. Geng, C. Girit, A. Zettl, M. F. Crommie, R. A. Segalman, S. G. Louie, and F. Wang, Nature (London) **471**, 617 (2011).

[11] T. Ando, J. Phys. Soc. Jpn. **75**, 124701 (2006).

[12] T. Ando, J. Phys. Soc. Jpn. **76**, 104711 (2007).

[13] A. B. Kuzmenko, L. Benfatto, E. Cappelluti, I. Crassee, D. van der Marel, P. Blake, K. S. Novoselov, and A. K. Geim, Phys. Rev. Lett. **103**, 116804 (2009).

[14] T.- Ta Tang, Y. Zhang, Ch.-H. Park, B. Geng, C. Girit, Z. Hao, M. C. Martin, A. Zettl, M. F. Crommie, S. G. Louie, Y. R. Shen, and F. Wang, Nat. Nanotech. **5**, 32 (2009).

[15] M. J. Rice, Phys. Rev. B **37**, 36 (1976).

[16] M. J. Rice and H.-Y. Choi, Phys. Rev. B **45**, 10173 (1992).

[17] T. Stauber, N. M. R. Peres, and A. H. Castro Neto, Phys. Rev. B **78**, 085418 (2008).

[18] J. P. Carbotte, E. J. Nicol, and S. G. Sharapov, Phys. Rev. B **81**, 045419 (2010).

[19] E. Cappelluti, L. Benfatto, and A. B. Kuzmenko, Phys. Rev. B **82**, 041402 (2010).

[20] U. Fano, Phys. Rev. **124**, 1866 (1961).

[21] M. Manzardo, E. Cappelluti, E. van Heumen, and A. B. Kuzmenko, Phys. Rev. B **86**, 054302 (2012).

[22] Z. Li, C. H. Lui, E. Cappelluti, L. Benfatto, K. F. Mak, G. L. Carr, J. Shan, and T. F. Heinz, Phys. Rev. Lett. **108**, 156801 (2012).

[23] T. Ando and M. Koshino, J. Phys. Soc. Jpn. **78**, 034709 (2009).

[24]P. Gava, M. Lazzeri, A. M. Saitta, and F. Mauri, Phys. Rev. B **80**, 155422 (2009).

[25]S. Piscanec, M. Lazzeri, F. Mauri, A. C. Ferrari, and J. Robertson, Phys. Rev. Lett. **93**, 185503 (2004).

[26]M. Lazzeri, C. Attaccalite, L. Wirtz, and F. Mauri, Phys. Rev. B **78**, 081406 (2008).

[27]E. J. Nicol and J. P. Carbotte, Phys. Rev. B **77**, 155409 (2008).

[28]A. B. Kuzmenko, E. van Heumen, D. van der Marel, P. Lerch, P. Blake, K. S. Novoselov, and A. K. Geim, Phys. Rev. B **79**, 115441 (2009).

[29]K. F. Mak, C. H. Lui, J. Shan, and T. F. Heinz, Phys. Rev. Lett. **102**, 256405 (2009).

[30]Y. Zhang, T.-T. Tang, C. Girit, Z. Hao, M. C. Martin, A. Zettl, M. F. Crommie, Y. R. Shen, and F. Wang, Nature (London) **459**, 820 (2009).

[31]A. B. Kuzmenko, I. Crassee, D. van der Marel, P. Blake, and K. S. Novoselov, Phys. Rev. B **80**, 165406 (2009).

[32]J. Yan, T. Villarson, E. A. Henriksen, P. Kim, and A. Pinczuk, Phys. Rev. B **80**, 241417(R) (2009).

[33]C. Thomsen, in *Light Scattering in Solids VI*, edited by M. Cardona and G. Guntherodt, (Springer, Berlin, 1991).

[34]For the sake of simplicity, we include herein a phenomenological constant term η responsible for all the damping processes arising from different sources of scattering, i.e., disorder/impurities, electron-electron, and electron-lattice interaction.

[35]We remind here that the vanishing of χ_{jA} in the undoped bilayer graphene, and hence of the phonon activity of this mode, is true if additional terms in the tight-binding Hamiltonian, such as the crystal field or the γ_3, γ_4 hopping parameters, are neglected. A more detailed discussion of this issue is provided in Sec. VI.

[36]R. J. Nemanich, G. Lucovsky, and S. A. Solin, Solid State Commun. **23**, 117 (1977).

[37]C. Underhill, S. Y. Leung, G. Dresselhaus, and M. S. Dresselhaus, Solid State Commun. **29**, 769 (1979).

[38]B. Partoens and F. M. Peeters, Phys. Rev. B **74**, 075404 (2006).

[39]E. Cappelluti and G. Profeta, Phys. Rev. B **85**, 205436 (2012).

[40]D. M. Basko, Phys. Rev. B **78**, 125418 (2008).

[41]D. M. Basko, New J. Phys. **11**, 095011 (2009).

[42]T. P. Devereaux and R. Hackl, Rev. Mod. Phys. **79**, 175 (2007).

[43]E. V. Castro, N. M. R. Peres, T. Stauber, and N. A. P. Silva, Phys. Rev. Lett. **100**, 186803 (2008).

[44]O. Vafek and K. Yang, Phys. Rev. B **81**, 041401 (2010).

[45]F. Zhang, H. Min, M. Polini, and A. H. MacDonald, Phys. Rev. B **81**, 041402 (2010).

[46]R. Nandkishore and L. Levitov, Phys. Rev. B **82**, 115124 (2010).

[47]M. Mucha-Kruczyński, I. L. Aleiner, and V. I. Fal'ko, Phys. Rev. B **84**, 041404 (2011).

[48]G. M. Rutter, S. Jung, N. N. Klimov, D. B. Newell, N. B. Zhitenev, and J. A. Stroscio, Nat. Phys. **7**, 649 (2011).

[49]L. A. Ponomarenko, A. K. Geim, A. A. Zhukov, R. Jalil, S. V. Morozov, K. S. Novoselov, I. V. Grigorieva, E. H. Hill, V. V. Cheianov, V. I. Fal'ko, K. Watanabe, T. Taniguchi, and R. V. Gorbachev, Nat. Phys. **7**, 658 (2011).

[50]D. S. L. Abergel and V. I. Fal'ko, Phys. Rev. B **86**, 041410 (2012).

[51]C. Lee, H. Yan, L. E. Brus, T. F. Heinz, J. Hone, and S. Ryu, ACS Nano **4**, 2695 (2010).

[52]A. D. LaForge, A. Frenzel, B. C. Pursley, T. Lin, X. Liu, J. Shi, and D. N. Basov, Phys. Rev. B **81**, 125120 (2010).

[53]L. Chauvière, Y. Gallais, M. Cazayous, M. A. Méasson, A. Sacuto, D. Colson, and A. Forget, Phys. Rev. B **84**, 104508 (2011).